A comparison of the Jacobian-free Newton-Krylov method and the EVP model for solving the sea ice momentum equation with a viscous-plastic formulation: a serial algorithm study

Jean-François Lemieux[a,*], Dana Knoll[b], Bruno Tremblay[c], David M. Holland[d], Martin Losch[e]

[a]*Recherche en Prévision Numérique environnementale/Environnement Canada, 2121 route Transcanadienne, Dorval, Qc H9P 1J3, Canada*
[b]*Los Alamos National Laboratory, P.O. Box 1663, Los Alamos, NM 87545, USA*
[c]*Department of Atmospheric and Oceanic Sciences, McGill University, 805 Sherbrooke Street West, Montréal, Qc H3A 2K6, Canada*
[d]*Courant Institute of Mathematical Sciences, New York University, 251 Mercer Street, New York, NY 10012-1185, USA*
[e]*Alfred-Wegener-Institut für Polar-und Meeresforschung, Postfach 120161, 27515, Germany*

Abstract

Numerical convergence properties of a recently developed Jacobian-free Newton-Krylov (JFNK) solver are compared to the ones of the widely used EVP model when solving the sea ice momentum equation with a Viscous-Plastic (VP) formulation. To do so, very accurate reference solutions are produced with an independent Picard solver with an advective time step of 10 s and a tight nonlinear convergence criterion on 10, 20, 40, and 80-km grids. Approximate solutions with the JFNK and EVP solvers are obtained for advective time steps of 10, 20 and 30 min. Because of an artificial elastic term, the EVP model permits an explicit time-stepping scheme with a relatively large subcycling time step. The elastic waves excited during the subcycling are intended to damp out and almost entirely disappear such that the approximate solution should be close to the VP solution. Results show that residual elastic waves cause the EVP approximate solution to have notable differences with the reference solution and that these differences get more important as the grid is refined. Compared to the reference solution, additional shear lines and zones of strong convergence/divergence are seen in

*Corresponding author
Email address: jean-francois.lemieux@ec.gc.ca (Jean-François Lemieux)

the EVP approximate solution. The approximate solution obtained with the JFNK solver is very close to the reference solution for all spatial resolutions tested.

Keywords: sea ice, viscous-plastic rheology, Newton-Krylov method, numerical convergence, numerical stability

1. Introduction

Sea ice dynamics plays an important role in shaping the ice cover in polar regions. Indeed, it strongly affects the sea ice thickness distribution which then influences the exchange of heat, moisture and momentum between the atmosphere and the underlying ocean.

To properly represent sea ice dynamics, it is crucial that rheology, i.e., the relationship between applied stresses and the resulting deformations, is correctly formulated. The very sporadic behavior of sea ice deformations suggests that critical stresses must be reached before the ice can fail in shear, compression or tension [1]. This lead modelers to consider sea ice as a plastic material (e.g., [1, 2]). Over the years, the constitutive law introduced by Hibler [2] has become the most widely used approach for the representation of the ice-ice interactions in sea ice models. When the ice is rigid, it is treated as a very viscous fluid [1]. However, once internal stresses reach critical values defined by a yield curve, the ice flows as a plastic material and can exhibit large deformations. This Viscous-Plastic (VP) constitutive law proposed by Hibler [2] is based on an elliptical yield curve and a normal flow rule (referred to as the standard VP rheology in this paper).

When using the elliptical yield curve with the parameters proposed by Hibler [2], sea ice can resist large stresses in compression, significant shear stresses, and has very limited tensile strength. The standard VP rheology implies a large change in the internal stresses when going from a non-divergent

[1] This viscous regime originates from a mathematical regularization for small deformations. This regularization has nevertheless a certain physical validity as the average (in space or in time) of many small plastic deformations has been shown to exhibit a viscous behavior [3].

velocity field to a slightly converging one (same idea in shear). This explains why a VP formulation leads to a very nonlinear problem that requires an efficient and robust numerical solver. The fact that the ice is treated as a very viscous fluid in zones of small deformations further complicates the problem. Indeed, a stability analysis shows that the time step required for an explicit time-stepping scheme is on the order of a second for a 100-km resolution grid [4] and a 100^{th} of a second for a resolution of 10 km, a typical spatial resolution for current regional models. Because of this stringent stability condition, Hibler [2] initially proposed to solve the momentum equation implicitly.

The numerical scheme introduced by Hibler [2] for solving the momentum equation is based on an implicit solution of a linearized system of equations and an outer loop (OL) iteration [2]. Hibler [2] initially proposed to perform 2 OL iterations at each time level. As the nonlinearities are not converged with only 2 OL iterations, the approximate solution responds slowly to changes in the wind forcing unless a small time step is used [2, 7]. However, as the number of OL increases, the approximate solution converges toward the nonlinear solution [8].

In recent papers, we have studied the convergence behavior [8] of the standard Picard solver and compared its computational efficiency and robustness to the ones of a newly developed Jacobian-Free Newton-Krylov (JFNK) solver [9]. Our conclusion is that the Picard solver converges very slowly. A large number of OL iterations are needed to obtain the fully-converged nonlinear solution and the number of OL iterations required is roughly multiplied by two when doubling the spatial resolution. Large errors (the largest errors coincide with the largest deformations) exist in the approximate solution if the number of OL iterations is insufficient. For a set of test cases and termination criteria, the JFNK solver is 3-7 times faster than the Picard solver. Importantly, this computational gain of JFNK over Picard increases with resolution and when a more accurate nonlinear solution is needed.

Current sea ice models are almost entirely based on a VP formulation.

[2] Sea ice modelers sometimes refer to the OL iterations as pseudo time steps [5] while it is customary in many other fields to refer to these as Picard iterations and to refer to this scheme as a Picard solver (e.g., [6]).

However, many modelers have in the past few years adopted a new approach for solving the momentum equation: the Elastic-Viscous-Plastic (EVP) model. Hunke and Dukowicz [10] added an artificial elastic term to the VP constitutive equation in order to relax the stability condition for an explicit time-stepping scheme. This approach leads to an explicit scheme using a relatively large time step (on the order of 10 s). Because the EVP is an explicit scheme, it is naturally suited for parallel computations and has demonstrated very good scaling with the number of processors [7]. In this first version of the EVP solver, the viscous coefficients were held at the previous time level and therefore not updated during the subcycling (the time-stepping is referred to as subcycling). This treatment leads to unphysical internal stresses lying outside of the yield curve [7]. To cure this problem, Hunke [11] proposed to include the viscous coefficients in the subcycling loop. To avoid the increase in floating point operations with this new EVP scheme, Young's modulus was redefined in terms of a damping time scale, which allowed a rearrangement of the stress equation such that the new EVP model is roughly as efficient as the first version [11]. The basic idea of the EVP scheme is to approximate the VP solution by damping the artificial elastic waves during the subcycling. Elastic waves disappear entirely in regions of lower ice concentration but remain in the solution where the ice concentration is very high, that is, where the ice should be nearly rigid and the VP solution must be regularized [11].

Recently, it has been pointed out, however, that the solution obtained with the EVP scheme is quite different that the one obtained with a Picard solver. Comparing results from a Picard solver with 2 OL iterations to the ones of the EVP with either 120 or 400 subcycles, Losch et al. [12] showed that the difference between these two can be larger than other effects: for example the effect of lateral boundary conditions and ice-ocean stress formulation, the choice of rheology (other yield curves) or advection scheme. As both solutions are approximate solutions, it was not possible for Losch et al. [12] to assert which one is better. Using idealized geometry, Losch and Danilov [13] concluded that the implicit and EVP approximate solutions can differ significantly because the EVP approximate solution tends to have smaller viscosities, especially in the vicinity of lateral boundaries and marginally resolved flow.

In this study, we investigate the numerical convergence properties of the EVP model and compare them to the ones of our JFNK solver. More specifi-

cally, we study the accuracy of the solution and the computational efficiency. We define a reference VP solution (calculated with an independent solver) to which we compare the JFNK and EVP approximate solutions. We also look at the impact of residual errors, in both the EVP and JFNK approximate solutions, on the simulation of sea ice deformations. The EVP model described in Hunke [11] is implemented (see also [14]). Additionally, we introduce a slightly different EVP solver by adding an extra inertial term to the momentum equation. This is done in order to get exactly the same solution as the implicit solver and to be able to define a residual. Reducing the residual to zero with this modified EVP solver ensures that the elastic waves have disappeared. Furthermore, this new approach can be used for validating an implementation of the EVP solver.

Even though the elastic component in the EVP model was first introduced as a numerical artifice, some argue that, the EVP approach can be considered a different rheology whose derivation is based on VP but that only approximates it, because of EVPs different regularization by elastic waves (E. Hunke, personal communication). Exploring the physical validity of the EVP approach is beyond the scope of this paper. It is possible that the regularization by elastic waves leads to a physically realistic solution when the ice is in a quasi-rigid state. However, large undamped elastic waves have been observed to lead to unphysical solutions in some circumstances. For example, in order to model landfast ice, Konig Beatty and Holland [15] added isotropic tensile strength by shifting the elliptical yield curve into the first quadrant. Their simulated landfast ice solution was very close to predictions by theory when they used a Picard solver, but they were not able to obtain a stable landfast ice with the EVP approach, because of residual elastic waves. In this paper, we consider the elastic term as a numerical technique: we investigate the use of two solvers (the EVP and JFNK schemes) for solving the momentum equation with the standard VP rheology. If the EVP approach were interpreted as a new and different rheology, our results would illustrate the differences between VP solutions and similar EVP solutions.

It is also important to mention that recent work has questioned the validity of the standard VP rheology. Indeed, the standard VP rheology has been shown to underestimate the deformations [16], the simulated shear lines are too broad compared to observations and do not significantly refine as the spatial resolution is increased [17], and statistics of deformations do not

match observations [18, 19] in both space and time [20]. While some authors propose very different constitutive laws to better represent the deformations (e.g., [19, 21]), others argue that a VP formulation requires a different yield curve and a different flow rule to improve its representation of sea ice deformations [17]. To study these new rheologies, accurate, robust and efficient solvers are needed. It is the topic of this paper to investigate the behavior of two numerical schemes for solving the sea ice momentum equation with the standard VP rheology. Nevertheless, our findings can still provide some informations on how these solvers would behave for other rheologies (especially for the other VP rheologies).

The contributions of this paper are: a thorough investigation of the convergence properties of the EVP model and their comparison with the ones of a JFNK solver, an investigation of the differences in the approximate solutions obtained with the EVP model and JFNK solver in the context of short term simulations, and a new formulation for the EVP solver that leads to exactly the same solution obtained with an implicit solver.

This paper is structured as follows. Section 2 describes the sea ice momentum equation with a VP formulation and the continuity equation. In section 3, the discretization of the momentum and continuity equations and the description of the solvers is presented. In section 4, we provide information about the model and describe the forcing fields and the initial conditions used for the simulations. A validation of our EVP model implementation is presented in section 5. The experiments performed are outlined in section 6. A discussion is provided in section 7. Concluding remarks are found in section 8.

2. Sea ice momentum and continuity equations

Because of the large ratio between the horizontal and the vertical scales $\mathrm{O}(1000\ \mathrm{km}/10\ \mathrm{m}) = \mathrm{O}(10^5)$, sea ice dynamics is often considered to be a two-dimensional problem [1]. The two-dimensional sea ice momentum equation is given by

$$\rho h \frac{D\mathbf{u}}{Dt} = -\rho h f \mathbf{k} \times \mathbf{u} + \tau_a - \tau_w + \nabla \cdot \sigma - \rho h g \nabla H_d, \tag{1}$$

where ρ is the density of the ice, h is the ice volume per unit area (or the mean thickness and just referred to as thickness in this paper), $\frac{D}{Dt}$ is the total derivative, f the Coriolis parameter, $\mathbf{u} = u\mathbf{i} + v\mathbf{j}$ the horizontal sea ice velocity vector, $\mathbf{i}$, $\mathbf{j}$ and $\mathbf{k}$ are unit vectors aligned with the x, y and z axis of our Cartesian coordinates, τ_a is the wind stress, τ_w the water drag, σ the internal ice stress tensor ($\nabla \cdot \sigma$ is defined as the rheology term), g the gravity and H_d the sea surface height. We follow Tremblay and Mysak [22], and express the sea surface tilt in terms of the geostrophic ocean current. With a simple quadratic law and constant turning angles θ_a and θ_w, τ_a and τ_w are expressed as [23]

$$\tau_{\mathbf{a}} = \rho_a C_{da} |\mathbf{u}_a^g| (\mathbf{u}_a^g \cos\theta_a + \mathbf{k} \times \mathbf{u}_a^g \sin\theta_a), \tag{2}$$

$$\tau_{\mathbf{w}} = C_w [(\mathbf{u} - \mathbf{u}_w^g) \cos\theta_w + \mathbf{k} \times (\mathbf{u} - \mathbf{u}_w^g) \sin\theta_w], \tag{3}$$

where $C_w = \rho_w C_{dw} |\mathbf{u} - \mathbf{u}_w^g|$, ρ_a and ρ_w are the air and water densities, C_{da} and C_{dw} are the air and water drag coefficients, and $\mathbf{u}_a^g$ and $\mathbf{u}_w^g$ are the geostrophic wind and ocean current. Because $\mathbf{u}$ is much smaller than $\mathbf{u}_a^g$, $\mathbf{u}$ is neglected in the expression for the wind stress.

With a VP formulation, the constitutive law, that relates the internal stresses and the strain rates, can be written as [2]

$$\sigma_{ij} = 2\eta\dot{\epsilon}_{ij} + [\zeta - \eta]\dot{\epsilon}_{kk}\delta_{ij} - P\delta_{ij}/2, \quad i,j = 1,2, \tag{4}$$

where σ_{ij} are the components of the ice stress tensor, δ_{ij} is the Kronecker delta, $\dot{\epsilon}_{ij}$ are the strain rates defined by $\dot{\epsilon}_{11} = \frac{\partial u}{\partial x}$, $\dot{\epsilon}_{22} = \frac{\partial v}{\partial y}$ and $\dot{\epsilon}_{12} = \frac{1}{2}(\frac{\partial u}{\partial y} + \frac{\partial v}{\partial x})$, $\dot{\epsilon}_{kk} = \dot{\epsilon}_{11} + \dot{\epsilon}_{22}$, ζ is the bulk viscosity and η is the shear viscosity.

We use a simple two-thickness category model and express the ice strength P as

$$P = P^* h \exp[-C(1 - A)], \tag{5}$$

where P^* is the ice strength parameter, A is the sea ice concentration and C is the ice concentration parameter, an empirical constant characterizing the strong dependence of the compressive strength on sea ice concentration [2].

The rheology term ($\nabla \cdot \sigma$) depends on the yield curve and the flow rule, through the formulation of the bulk and shear viscosities. In the following, we use the elliptical yield curve with a normal flow rule [2]. In this case, the bulk and shear viscosities are given by

$$\zeta = \frac{P}{2\triangle}, \tag{6}$$

$$\eta = \zeta e^{-2}, \tag{7}$$

where $\triangle = [(\dot{\epsilon}_{11}^2 + \dot{\epsilon}_{22}^2)(1 + e^{-2}) + 4e^{-2}\dot{\epsilon}_{12}^2 + 2\dot{\epsilon}_{11}\dot{\epsilon}_{22}(1 - e^{-2})]^{\frac{1}{2}}$, and e is the ratio of the long axis and the short axis of the elliptical yield curve.

In the limit where $\triangle$ tends to zero, equations (6) and (7) become singular. To avoid this problem, ζ is capped using an hyperbolic tangent [8]

$$\zeta = \zeta_{max} \tanh(\frac{P}{2\triangle\zeta_{max}}). \tag{8}$$

As in equation (7), $\eta = \zeta e^{-2}$. The maximum bulk viscous coefficient ζ_{max} is set to the value proposed by Hibler [2]: $2.5 \times 10^8 P$ (which is equivalent to capping $\triangle$ to a minimum value of $2 \times 10^{-9}\mathrm{s}^{-1}$). As opposed to the regularization introduced by Hibler [2], this formulation for ζ is continuously differentiable for numerical purposes.

The continuity equations for the thickness (volume per unit area) and the concentration are given by

$$\frac{\partial h}{\partial t} + \nabla \cdot (h\mathbf{u}) = S_h, \tag{9}$$

$$\frac{\partial A}{\partial t} + \nabla \cdot (A\mathbf{u}) = S_A, \tag{10}$$

where S_h and S_A are thermodynamic source terms. These source terms are set to zero in the simulations described in this paper (unless otherwise stated) as we concentrate on matters related to the dynamics.

3. Numerical approaches

3.1. Temporal and spatial discretizations

Following Zhang and Hibler [5] and Hunke [11], the advection of momentum is neglected because this term is very small compared to the other ones in the momentum equation. The momentum and continuity equations are solved at time levels Δt, $2\Delta t$, $3\Delta t, \ldots$ where Δt is referred to as the advective time step and the index $n = 1, 2, 3, \ldots$ refers to these time levels. As done in most sea ice models (e.g., [2, 10, 22]) a splitting in time is used between the momentum and the continuity equations. This splitting implies that h and A are considered to be known in the momentum equation as they are held at the previous time level. Hence, the u and v momentum equations at time level n are written as

$$\rho h^{n-1} \frac{\partial u}{\partial t}^{n} = \rho h^{n-1} f v^{n} - \tau_{wu}^{n} + \frac{\partial \sigma_{11}}{\partial x}^{n} + \frac{\partial \sigma_{12}}{\partial y}^{n} + r_{*u}^{n}, \tag{11}$$

$$\rho h^{n-1} \frac{\partial v^{n}}{\partial t} = -\rho h^{n-1} f u^{n} - \tau_{wv}^{n} + \frac{\partial \sigma_{22}}{\partial y}^{n} + \frac{\partial \sigma_{12}}{\partial x}^{n} + r_{*v}^{n}, \tag{12}$$

where r_{*u}^{n} and r_{*v}^{n} include the wind stress and the sea surface tilt for the u and the v equations. Note that as h and A are held at time n-1, the ice strength in the rheology term is also expressed with previous time level values. As the water drag and the rheology term are written in terms of the velocity field, the only unknowns in equations (11) and (12) are u^{n} and v^{n}.

The components of the velocity (u and v) are positioned on the Arakawa C-grid (the four corners and the middle of the cell are respectively referred to as the nodes and the tracer point). A Dirichlet boundary condition is applied at an ocean-land boundary ($u = 0$, $v = 0$) and a Neumann condition at an open boundary (i.e., the spatial derivatives of the components of velocity in the normal direction with the open boundary are chosen to be zero). For stability, the ice strength P is set to zero at the open boundaries [24]. A f-plane approximation is used with $f = 1.46 \times 10^{-4}\mathrm{s}^{-1}$. Spatial derivatives (in the rheology term) are discretized using centered finite differences except close to land boundaries where second order accurate Taylor series expansions are used. Viscous coefficients are calculated directly from the velocity field at the tracer point and at the grid node (as both of these locations are needed to calculate the complete rheology term). The spatial discretization

(with nx tracer points in one direction and ny in the other one) leads to a system of $N = (ny(nx+1) + nx(ny+1))$ nonlinear equations for the velocity components. Once these equations are solved for u^n and v^n everywhere on the grid, the thickness and concentration fields are advanced in time by solving:

$$\frac{\partial h}{\partial t}^n + \nabla \cdot (h^{n-1}\mathbf{u}^n) = 0, \tag{13}$$

$$\frac{\partial A}{\partial t}^n + \nabla \cdot (A^{n-1}\mathbf{u}^n) = 0. \tag{14}$$

A forward Euler approach is used for the first term of equations (13) and (14) along with a simple upstream advection scheme (as done in [22]). We now focus on solving the momentum equation, keeping in mind the splitting in time of the momentum and continuity equations. We therefore drop the superscript for h, A and P which are considered known quantities when solving the momentum equation.

3.2. The JFNK solver

We give a brief overview of the JFNK implementation. More details can be found in Lemieux et al. [9] and Lemieux et al. [25].

Following Zhang and Hibler [5], the inertial term at time level n is expressed using a backward Euler differencing. Equations (11) and (12) can therefore be written as

$$\rho h \frac{(u^n - u^{n-1})}{\Delta t} = \rho h f v^n_{avg} - \tau^n_{wu} + \frac{\partial \sigma^n_{11}}{\partial x} + \frac{\partial \sigma^n_{12}}{\partial y} + r^n_{*u}, \tag{15}$$

$$\rho h \frac{(v^n - v^{n-1})}{\Delta t} = -\rho h f u^n_{avg} - \tau^n_{wv} + \frac{\partial \sigma^n_{22}}{\partial y} + \frac{\partial \sigma^n_{12}}{\partial x} + r^n_{*v}, \tag{16}$$

where v_{avg} is the average of the four v components of velocity surrounding a u location on the C-grid (same idea for u_{avg}) and the components of the internal stress tensor are given by

$$\sigma^n_{11} = \zeta^n(\frac{\partial u^n}{\partial x} + \frac{\partial v^n}{\partial y}) + \eta^n(\frac{\partial u^n}{\partial x} - \frac{\partial v^n}{\partial y}) - \frac{P}{2}, \tag{17}$$

$$\sigma_{22}^n = \zeta^n(\frac{\partial v^n}{\partial y} + \frac{\partial u^n}{\partial x}) + \eta^n(\frac{\partial v^n}{\partial y} - \frac{\partial u^n}{\partial x}) - \frac{P}{2}, \tag{18}$$

$$\sigma_{12}^n = \eta^n(\frac{\partial u^n}{\partial y} + \frac{\partial v^n}{\partial x}). \tag{19}$$

Expanding the water drag and rearranging the terms, equations (15) and (16) can be written as

$$\begin{aligned}\rho h\frac{u^n}{\Delta t} - \rho h f v_{avg}^n + C_w^n(u^n\cos\theta_w - v_{avg}^n\sin\theta_w) - \frac{\partial\sigma_{11}^n}{\partial x} - \frac{\partial\sigma_{12}^n}{\partial y} = \\ \rho h\frac{u^{n-1}}{\Delta t} + C_w^n(u_w^g\cos\theta_w - v_w^g\sin\theta_w) + r_{*u}^n,\end{aligned} \tag{20}$$

$$\begin{aligned}\rho h\frac{v^n}{\Delta t} + \rho h f u_{avg}^n + C_w^n(v^n\cos\theta_w + u_{avg}^n\sin\theta_w) - \frac{\partial\sigma_{22}^n}{\partial x} - \frac{\partial\sigma_{12}^n}{\partial y} = \\ \rho h\frac{v^{n-1}}{\Delta t} + C_w^n(v_w^g\cos\theta_w + u_w^g\sin\theta_w) + r_{*v}^n.\end{aligned} \tag{21}$$

Using equations (17), (18) and (19), the only unknowns in equations (20) and (21) are u^n and v^n. The spatial discretization of equations (20) and (21) leads to a system of N nonlinear equations with N unknowns that can be concisely written as

$$\mathbf{A}(\mathbf{u}^n)\mathbf{u}^n = \mathbf{b}(\mathbf{u}^n), \tag{22}$$

where $\mathbf{A}$ is an $N \times N$ matrix. The vector $\mathbf{u}^n$ is formed by stacking first the u components followed by the v components. Similarly, the vector $\mathbf{b}$ is a function of the velocity vector $\mathbf{u}^n$ because of C_w^n. We drop the superscript n knowing that we wish to find the solution $\mathbf{u} = \mathbf{u}^n$. We introduce the residual vector $\mathbf{F}(\mathbf{u})$:

$$\mathbf{F}(\mathbf{u}) = \mathbf{A}(\mathbf{u})\mathbf{u} - \mathbf{b}(\mathbf{u}). \tag{23}$$

The residual $\mathbf{F}(\mathbf{u})$ is useful as it allows one to assess the quality of the approximate solution because for $\mathbf{F}(\mathbf{u}) = 0$ the solution is fully converged.

The basic idea of implicit methods for solving a nonlinear system of equations is to solve a series of linear systems of equations until this series converges to the solution $\mathbf{u}$. The solutions of these linear systems of equations are called iterates and are represented by $\mathbf{u}^1$, $\mathbf{u}^2 ... \mathbf{u}^k$ where the superscript denotes the iterate number (not to be confused with the time level).

The Newton method for solving the nonlinear system of equations (22) is based on a multivariate Taylor expansion around a previous iterate $\mathbf{u}^{k-1}$:

$$\mathbf{F}(\mathbf{u}^{k-1} + \delta\mathbf{u}^k) \approx \mathbf{F}(\mathbf{u}^{k-1}) + \mathbf{F}'(\mathbf{u}^{k-1})\delta\mathbf{u}^k. \tag{24}$$

The higher order terms are neglected in the expression above. Setting $\mathbf{F}(\mathbf{u}^{k-1} + \delta\mathbf{u}^k) = 0$, the correction $\delta\mathbf{u}^k = \mathbf{u}^k - \mathbf{u}^{k-1}$ can be obtained by solving the linear system of N equations:

$$\mathbf{J}(\mathbf{u}^{k-1})\delta\mathbf{u}^k = -\mathbf{F}(\mathbf{u}^{k-1}), \tag{25}$$

where the system matrix $\mathbf{J} \equiv \mathbf{F}'$ is the Jacobian, an $N \times N$ matrix whose entries are $J_{qr} = \partial F_q(\mathbf{u}^{k-1})/\partial(u_r^{k-1})$ (where $q = 1, N$ and $r = 1, N$). For $k = 1$, an initial iterate $\mathbf{u}^0$ needs to be provided. The initial iterate that we use is the previous time step solution $\mathbf{u}^{n-1}$. Once the linear system of equations (25) is solved, the next iterate is given by

$$\mathbf{u}^k = \mathbf{u}^{k-1} + \delta\mathbf{u}^k, \tag{26}$$

Obtaining the Jacobian matrix in equation (25) is a very difficult development task. However, because a Krylov method is used for the linear solver, it is possible to avoid forming the Jacobian. Krylov methods approximate the solution in a subspace of the form $(\mathbf{r}_0, \mathbf{J}\mathbf{r}_0, \mathbf{J}^2\mathbf{r}_0 ...)$ where $\mathbf{r}_0 = \mathbf{J}(\mathbf{u}^{k-1})\delta\mathbf{u}_0^k + \mathbf{F}(\mathbf{u}^{k-1})$ is the initial residual of the linear system of equations. The vector $\delta\mathbf{u}_0^k$ is the initial guess of the linear system of equations and is usually taken to be zero. This implies that $\mathbf{r}_0 = \mathbf{F}(\mathbf{u}^{k-1})$. When creating the subspace, Krylov methods only require the product of the Jacobian and a vector. This means that the Jacobian does not need to be formed directly: only its action on a vector is required. This is fundamental for implementing a Jacobian-free approach as $\mathbf{J}(\mathbf{u}^{k-1})$ times a certain vector $\mathbf{w}$ can be approximated by a first-order Taylor series expansion [26]

$$\mathbf{J}(\mathbf{u}^{k-1})\mathbf{w} \sim \frac{\mathbf{F}(\mathbf{u}^{k-1} + \epsilon\mathbf{w}) - \mathbf{F}(\mathbf{u}^{k-1})}{\epsilon}, \tag{27}$$

where $\mathbf{w}$ is a vector needed to form the Krylov subspace (e.g., $\mathbf{r}_0$) and ϵ is a small number (10^{-6} in this implementation).

The Krylov method that we use for the linear solve is the Flexible Generalized Minimum RESidual (FGMRES, [27]). A Krylov method for solving a linear system of equations such as the one described in equation (25) is likely to exhibit a very low convergence rate (and possibly robustness issues). To accelerate the convergence rate of each linear solve, preconditioning is used. Preconditioning transforms the system of equations in a form that is easier to solve but that still has the same solution as the original system. The preconditioning operator that we use is the same used for our Picard solver and involves 10 iterations of a Line Successive Over Relaxation (LSOR) solver similar to the one implemented by Zhang and Hibler [5] (they use it as a solver however, not as a preconditioner). The transformed system of equations becomes

$$\mathbf{J}(\mathbf{u}^{k-1})\mathbf{P}^{-\mathbf{1}}\delta\mathbf{z} = -\mathbf{F}(\mathbf{u}^{k-1}), \tag{28}$$

where $\delta\mathbf{z} = \mathbf{P}\delta\mathbf{u}^k$ and $\mathbf{P}^{-\mathbf{1}}$ is referred to as the preconditioning operator.

We use an inexact Newton method [28] to improve robustness and computational efficiency. The idea is to solve the linear system of equations with a loose tolerance in early Newton iterations and progressively tighten up the tolerance as the nonlinear solution is approached. The preconditioned FGMRES method solves the linear system of equations until the residual is smaller than $\gamma(k) \parallel \mathbf{F}(\mathbf{u}^{k-1}) \parallel$ where $\parallel \parallel$ is the L2-norm and $\gamma(k)$ is the tolerance of the linear solver at iteration k (a value smaller than 1). The tolerance of the linear solver with this inexact Newton approach is given by

$$\gamma(k) = \begin{cases} \gamma_{ini}, & \text{if } ||\mathbf{F}(\mathbf{u^{k-1}})|| \geq \text{res}_t, \\ \frac{||\mathbf{F}(\mathbf{u^{k-1}})||}{||\mathbf{F}(\mathbf{u^{k-2}})||}, & \text{if } ||\mathbf{F}(\mathbf{u^{k-1}})|| < \text{res}_t. \end{cases} \tag{29}$$

The tolerance γ_{ini} for the initial stage is set to 0.99. Hence, the tolerance is very loose in early Newton iterations (until the L2-norm reaches a value of res_t) and later is calculated from previous values of the L2-norm. The parameter res_t is the only value that changes with the spatial resolution; it is set to 0.05 at 80-km resolution, 0.25 at 40 km, 0.625 at 20 km and 1.25 at 10 km. These values were chosen in order to get a compromise between robustness and computational efficiency. The tolerance $\gamma(k)$ is also forced to

be larger than 0.1 to prevent excessive use of the linear solver which tends to slow down the nonlinear solver.

Finally, a termination criterion (defined by γ_{nl}) for solving the nonlinear system of equations also needs to be given. Hence, the JFNK solver stops iterating after a required drop in the nonlinear L2-norm: when the L2-norm is γ_{nl} times smaller than the initial L2-norm $||\mathbf{F}(\mathbf{u^0})||$. JFNK fails to converge when the termination criterion is not reached in $k_{max} = 200$ iterations. Compared to our first JFNK version [9], our current JFNK solver is more robust for the following two reasons. First, the viscous coefficients are now calculated independently at the tracer and at the node points. In our first version, the viscous coefficients were calculated at the tracer points and then averaged to obtain the value at the grid node (which is inconsistent because of the nonlinear relation). Second, the robustness is improved by setting back the linear tolerance to γ_{ini} when $k > 100$ (this approach allows the nonlinear residual to decrease again when it sometimes flattens out and oscillates in the first 100 iterations). We will come back to robustness issues of the JFNK solver later in this paper.

Note that developing a JFNK solver from an existing implicit Picard solver (e.g., [2] or [5]) is relatively straightforward as the linear solver can be used as is for the preconditioning step and the residual vector can be obtained from the same linear solver code with minor modifications. Krylov solver routines (such as FGMRES) are available in many software libraries (e.g, [29]).

3.3. The EVP solver

The EVP model also solves the momentum equations (11) and (12) at time level n. The forcing r_{*u} and r_{*v} are again at level n and the same splitting in time approach between the momentum and continuity equations is used such that A, h and the ice strength P are held at time level n-1.

The velocity field at time level n is obtained with the EVP by solving explicitly the momentum equation from time n-1 to time n. This time integration is often referred to as a subcycling of the larger advective time step Δt. We denote the subcycling here with the superscript s. At iteration s of

the subcycling loop, the solution is advanced from s-1 to s.

Hunke and Dukowicz [10] noticed that equation (4) can alternatively be expressed as

$$\frac{1}{2\eta}\sigma_{ij} + \frac{\eta-\zeta}{4\eta\zeta}\sigma_{kk}\delta_{ij} + \frac{P}{4\zeta}\delta_{ij} = \dot{\epsilon}_{ij}. \tag{30}$$

Adding an artificial elastic strain with an elastic parameter E, we get

$$\frac{1}{E}\frac{\partial\sigma_{ij}}{\partial t} + \frac{1}{2\eta}\sigma_{ij} + \frac{\eta-\zeta}{4\eta\zeta}\sigma_{kk}\delta_{ij} + \frac{P}{4\zeta}\delta_{ij} = \dot{\epsilon}_{ij}. \tag{31}$$

Introducing $T = \zeta/E$ [11], equation (31) can be written as

$$\frac{\partial\sigma_{ij}}{\partial t} + \frac{e^2}{2T}\sigma_{ij} + \frac{1-e^2}{4T}\sigma_{kk}\delta_{ij} + \frac{P}{4T}\delta_{ij} = \frac{\zeta}{T}\dot{\epsilon}_{ij}. \tag{32}$$

Following equation (32), the component of the stress tensor are time stepped (using the velocity field at time s-1) according to

$$\frac{(\sigma_1^s - \sigma_1^{s-1})}{\Delta t_e} + \frac{\sigma_1^s}{2T} = \frac{\zeta^{s-1}(\dot{\epsilon}_{11}^{s-1} + \dot{\epsilon}_{22}^{s-1})}{T} - \frac{P}{2T}, \tag{33}$$

$$\frac{(\sigma_2^s - \sigma_2^{s-1})}{\Delta t_e} + \frac{e^2\sigma_2^s}{2T} = \frac{\zeta^{s-1}(\dot{\epsilon}_{11}^{s-1} - \dot{\epsilon}_{22}^{s-1})}{T}, \tag{34}$$

$$\frac{(\sigma_{12}^s - \sigma_{12}^{s-1})}{\Delta t_e} + \frac{e^2\sigma_{12}^s}{2T} = \frac{\zeta^{s-1}\dot{\epsilon}_{12}^{s-1}}{T}, \tag{35}$$

where $\sigma_1 = \sigma_{11} + \sigma_{22}$, $\sigma_2 = \sigma_{11} - \sigma_{22}$, ζ^{s-1} is $\zeta\left(u^{s-1}, v^{s-1}\right)$ and for example $\dot{\epsilon}_{11} = \frac{\partial u^{s-1}}{\partial x}$. T is a tuning parameter and represents a damping timescale for the elastic waves. It is a fraction of the advective time step and is set to $0.36\Delta t$ (unless otherwise stated) following the documentation of the CICE model [14]. The EVP subcycling time step is denoted by Δt_e. In the standard EVP model, $N_{sub} * \Delta t_e = \Delta t$ where N_{sub} is the number of subcycles. The viscous coefficients are in our implementation also calculated following equation (8).

With the newly calculated stresses, the velocity is then subcycled according to

$$\rho h \frac{(u^s - u^{s-1})}{\Delta t_e} =$$
$$\rho h f v^{s-1}_{avg} + C^s_w((u^g_w - u^s)\cos\theta_w - (v^g_w - v^{s-1}_{avg})\sin\theta_w) + \frac{\partial \sigma^s_{11}}{\partial x} + \frac{\partial \sigma^s_{12}}{\partial y} + r^n_{*u}, \tag{36}$$

$$\rho h \frac{(v^s - v^{s-1})}{\Delta t_e} =$$
$$-\rho h f u^{s-1}_{avg} + C^s_w((v^g_w - v^s)\cos\theta_w + (u^g_w - u^{s-1}_{avg})\sin\theta_w) + \frac{\partial \sigma^s_{22}}{\partial y} + \frac{\partial \sigma^s_{12}}{\partial x} + r^n_{*v}, \tag{37}$$

where $C^s_w = \rho_w C_{dw}|\mathbf{u}^{s-1} - \mathbf{u}^g_w|$ (calculated at the u or v C-grid positions).

The spatial discretization also leads to a system of N equations with N unknowns. Contrary to the B-grid implementation of Hunke [11], the off-diagonal terms (Coriolis and part of the water drag) are explicit (considered at s-1 and not s).

The basic idea of the EVP solver is to approximate the VP solution by damping the artificial elastic waves (with a T e-folding time scale) during the subcycling. The goal is therefore to attenuate the elastic waves as much as possible while maintaining numerical stability [11]. Hunke [11] performed a stability analysis for the EVP solver. Neglecting the water drag term and considering a linear problem (i.e. the rheology term is considered linear), this stability analysis shows that the elastic waves damp out and the approximate solution is stable if the following relation is respected

$$\Delta t_e < \frac{4e\Delta x}{(1+e^2)}(\frac{\rho h T}{\zeta})^{\frac{1}{2}}. \tag{38}$$

This relation indicates that zones characterized by high viscosities set a severe constraint on the value of Δt_e. It further shows that reducing the damping time scale implies a reduction of Δt_e to maintain stability and that the subcycling time step has to be decreased by a factor of two when doubling the spatial resolution. A method proposed by Hunke [11] to mitigate this stability issue is to limit the values of the viscous coefficients to enforce the

inequality in equation (38). As this approach is not recommended (E. Hunke, personal communication) and has never been used in actual applications of CICE, we have chosen not to study it in this paper.

3.4. The modified EVP approach

We propose a modification to the Hunke [11] scheme inspired by the work of a few groups in computational fluid dynamics (see for example [30]). We call this new solver EVP*. The times-stepping of the internal stresses is the same (see equations (33), (34) and (35)). However, we modify the time-stepping of the velocities: an extra inertial term is added in order to match the backward Euler of the implicit approach. Equations (36) and (37) become

$$\beta\frac{(u^s-u^{s-1})}{\Delta t_e}+\rho h\frac{(u^s-u^{n-1})}{\Delta t}= \\ \rho h f v^{s-1}_{avg}+C^s_w((u^g_w-u^s)\cos\theta_w-(v^g_w-v^{s-1}_{avg})\sin\theta_w)+\frac{\partial\sigma^s_{11}}{\partial x}+\frac{\partial\sigma^s_{12}}{\partial y}+r^n_{*u}, \tag{39}$$

$$\beta\frac{(v^s-v^{s-1})}{\Delta t_e}+\rho h\frac{(v^s-v^{n-1})}{\Delta t}= \\ -\rho h f u^{s-1}_{avg}+C^s_w((v^g_w-v^s)\cos\theta_w+(u^g_w-u^{s-1}_{avg})\sin\theta_w)+\frac{\partial\sigma^s_{22}}{\partial y}+\frac{\partial\sigma^s_{12}}{\partial x}+r^n_{*v}, \tag{40}$$

where β is a tuning parameter that can change spatially and with time.

Notice the presence in equations (39) and (40) of two time steps: the EVP subcycling time step and the advective time step Δt. These two equations are effectively subcycled with a time step of Δt_e but the condition $N_{sub} * \Delta t_e = \Delta t$ does not need to be respected. The basic idea is that once steady state is reached (within the same subcycling cycle of N_{sub} iterations), the first term goes to zero and u^s tends toward u^n. Because of the extra inertial term, once u^s tends toward u^n, the representation of the inertial term is exactly the same as for the implicit approach and one recovers exactly the same solution. One can see this by replacing u^s by u^n (same idea for v) and

dropping the first term in equations (39) and (40) and comparing these to equations (15) and (16).

The term $\rho h u^{n-1}/\Delta t$ in equation (39) is like a forcing term (does not change during the subcycling) and the term $\rho h u^{s}/\Delta t$ acts as a linear drag. Following Hunke [11] who neglected the drag term in the stability analysis, the condition for stability of EVP* is given by:

$$\Delta t_e < \frac{4e\Delta x}{(1+e^2)}(\frac{\beta T}{\zeta})^{\frac{1}{2}}. \tag{41}$$

Interestingly, if we set $\beta = \rho h$ in equations (39) and (40), we get exactly the same stability condition as the standard EVP solver. The parameter β is set to ρh for the experiments described in this paper.

There are advantages with this modified EVP approach: it can used to validate the implementation of the standard EVP solver, a residual can be calculated and the approximate solution obtained with this solver should tend toward the implicit solution if the residual tends toward zero.

4. Model information, forcing fields and initial conditions

Our regional model can be run at four possible spatial resolutions: 10, 20, 40 and 80 km (square grid cells). The domain includes the Arctic, the North Atlantic and the Canadian Arctic Archipelago (CAA). There are open channels in the CAA only for the 10 and 20-km resolution versions. The model uses two thickness categories and a zero-layer thermodynamics. A Neumann condition for the thickness and the concentration fields is applied at an open boundary by imposing spatial gradients equal to zero. The sea ice model is coupled thermodynamically to a slab ocean model [22].

The wind stress is calculated using the geostrophic winds derived from the National Centers for Environmental Prediction and National Center for Atmospheric Research (NCEP/NCAR) six hour reanalysis of sea level pressure [31]. The geostrophic winds at time level n are linearly interpolated between the previous and subsequent six hour geostrophic wind fields. The climatological ocean currents were obtained from the steady-state solution

of the Navier-Stokes equation in which the advection of momentum was neglected, a 2-D non-divergent field was assumed and a quadratic drag law was used. The forcing used to get the ocean currents is a 30-year climatological wind stress field. The thermodynamics is forced by NCEP/NCAR reanalysis of monthly mean surface air temperature. All NCEP/NCAR reanalysis data are found at www.esrl.noaa.gov.

Previous simulations with the Picard solver are used to obtain the initial conditions for the experiments described in this study. These simulations started with a uniform thickness of 1 m and a concentration of 100% and ran for 10 years (at each spatial resolution) from 1 January 1992 to 1 January 2002 with a two-hour time step. Starting from the fields obtained on 1 January 2002, the model was then run with a 20-min time step from 1 January 2002 to 17 January 2002 00Z. We now turn off the thermodynamics and compare the different solvers over the period 17 January 2002 00Z to 18 January 2002 00Z. The reason why we have chosen this specific 24-hour period is that it is characterized by typical conditions with a high pressure system close to the Beaufort Sea, convergence north of Greenland and ice flowing south through Fram Strait.

For all the experiments, we use revision 291 of our model. All runs were performed on a machine with 2 Intel E5520 quad-core CPU at 2.26 GHz with 8 MB of cache and 72 GB of RAM. The compiler is GNU fortran (GCC) 4.1.2 20080704 (Red Hat 4.1.2-51), 64 bits. The optimization option O3-ffast-math was used for all the runs.

Tables (1) and (2) list respectively the values of the physical and numerical parameters used for the core runs of the paper. Additional simulations are also described for which modification(s) to these parameters are stated clearly.

5. Validation of the EVP implementation

Experiments show that the EVP* solver sometimes does not converge when using the standard value of P* (27.5×10^3 N m^{-2}). When this occurs, the residual initially decreases but then flattens out. It is possible that improvements can be obtained by tuning the damping time scale T or the

Symbol	**Definition**	**value**
ρ	sea ice density	900 kg m^{-3}
ρ_a	air density	1.3 kg m^{-3}
ρ_w	water density	1026 kg m^{-3}
C_{da}	air drag coefficient	1.2×10^{-3}
C_{dw}	water drag coefficient	5.5×10^{-3}
θ_{da}	air drag turning angle	25°
θ_{dw}	water drag turning angle	25°
f	Coriolis parameter	$1.46 \times 10^{-4} s^{-1}$
P*	ice strength parameter	27.5×10^3 N m^{-2}
C	ice concentration parameter	20
e	ellipse ratio	2

Table 1: Physical parameters for the runs

Symbol	**Definition**	**value(s)**
Δx	spatial resolution	10, 20, 40, 80 km
Δt	advective time step	10, 20, 30 min
γ_{nl}	termination criterion	0.99 to 10^{-3}
N_{sub}	number of subcycling time steps	30 to 1920
T	elastic damping timescale	$0.36\Delta t$

Table 2: Numerical parameters for the runs

parameter β in equations (39) and (40), but this is not explored in this paper. Nevertheless, the EVP* solver represents a very useful validation tool for our EVP solver implementation. We test that a solution obtained with the EVP* solver is the same than the one obtained with the Picard solver when both solvers are iterated to full convergence. Passing this test gives us confidence that our implementation of EVP (from which the EVP* solver is derived with small code changes) is consistent with the Picard solver approach. Both Picard and JFNK implementations are very well tested softwares.

For this experiment, the spatial resolution is 40 km and the advective time step is 20 min. The thickness is set to 1 m everywhere on the domain and the concentration to 100%. To ensure numerical convergence, the ice strength is set to 27.5×10^2 N m^{-2} (an order of magnitude smaller than the standard value). We investigate the first time level on 17 January 2002. As the condition $N_{sub} * \Delta t_e = \Delta t$ does not need to be respected for the EVP* solver, N_{sub} and Δt_e are specified independently. In this experiment, a large number of subcycles are performed as we want to reach full-convergence. The black line on Figure 1 shows the L2-norm of the nonlinear system of equations when a subcycling time step of 30 s is used. Obviously, 30 s is a too large Δt_e as the approximate solution calculated by EVP* does not converge. Consistent with equation (41), a smaller subcycling time step ($\Delta t_e =$ 10 s) leads to convergence (blue curve). The flattening out of the curve after $\sim$4500 subcycles means that the solution has reached machine accuracy.

The velocity field for the same time level was also calculated using the Picard solver (not shown). The differences between the velocity field calculated with the EVP* solver and the one obtained using the Picard solver are O(10^{-16}cm s^{-1}), i.e. both solvers give the same answer, the small differences are due to the machine precision.

Figure 1: L2-norm for the EVP* solver with $\Delta t_e = 30s$ (in black) and $\Delta t_e = 10s$ (in blue). The time is 17 January 2002 00Z 20 min, the spatial resolution is 40 km and the advective time step is 20 min.

6. Experiments

For comparing the robustness and computational efficiency of a solver to the ones of another solver, it is important to define common metrics. It was easy for Lemieux et al. [9] to compare in a consistent way robustness and computational efficiency of the standard Picard solver and the newly developed JFNK solver as both solvers allow a calculation of the nonlinear residual. When decreasing the residual to zero (not exactly zero because of machine precision), both solvers give exactly the same answer (the velocity field at time level n).

In this work, we also have a residual for the EVP* solver. However, for the standard EVP model, a different metric is needed. Assuming both solvers (JFNK and EVP) find their respective fully converged velocity solution, we don't expect the velocity fields to be exactly the same because of the different treatment of the inertial term. Indeed, the error on the inertial term is $O(\Delta t_e)$ for the EVP while the backward Euler approach for JFNK exhibits an error of $O(\Delta t)$. In this sense, the EVP should be more accurate than JFNK.

For comparing the JFNK and EVP solvers, the Picard solver is used in order to get an independent solution. Lemieux and Tremblay [8] showed that the approximate solution obtained with the Picard solver converges to the VP solution when the residual tends toward zero. At each spatial resolution, a 1-day simulation (on 17 January 2002) was performed with the Picard solver with a very small advective time step (10 s) and a very tight nonlinear convergence criterion ($\gamma_{nl} = 10^{-6}$). The ice starts from rest and the wind is turned on on 17 January 2002 00Z. With such a small advective time step and the low value of γ_{nl} used, the velocity, concentration and thickness fields obtained on 18 January 2002 00Z form the reference solution. Note that the standard value of P* is used (27.5×10^3 N m^{-2}). The quality of the reference solution was assessed using the 40-km grid. Keeping $\gamma_{nl} = 10^{-6}$, the advective time step was reduced to 1 s. Subtracting this highly accurate solution (with Δt=1 s) from the reference solution (with Δt=10 s), the maximum thickness difference is 5×10^{-5} m and the maximum velocity difference is 1.1×10^{-3} cm s^{-1}.

Starting again from rest on 17 January 2002 00Z, the approximate solu-

tion is advanced in time in order to get the same fields on 18 January 2002 00Z with either the JFNK or the EVP solvers with a set of advective time steps and termination criteria (for JFNK) or number of subcycles (for the EVP). The thickness, velocity and deformation fields simulated by the JFNK solver and the EVP model are then compared with the reference solution. These experiments are performed at 10, 20, 40 and 80-km resolutions with advective time steps of 10, 20 and 30 minutes (typical time steps used in current regional ice-ocean models [32]).

The differences between the JFNK approximate solution and the reference solution are due to the $O(\Delta t)$ error of the backward Euler approach, the large advective time step and the residual errors associated with each solve of the momentum equation. The fields on 18 January 2002 00Z simulated by JFNK should tend toward the reference solution as Δt and γ_{nl} are reduced.

Similarly, the differences between the EVP approximate solution and the reference solution are due to the large advective time step and the residual errors caused by undamped elastic waves. Note that the error of the inertial term for the EVP is comparable to the error of the inertial term of the reference solution and is therefore negligible. We expect the fields on 18 January 2002 00Z simulated by the EVP model to approach the reference solution as Δt is reduced and as the number of subcycles N_{sub} is increased.

These experiments with different advective time steps and γ_{nl} (for JFNK) or N_{sub} (for EVP) will allow us to access the accuracy of the JFNK and EVP approximate solutions. The EVP solver is tested for the standard number of subcycles (120) proposed in the CICE documentation [14] as well by using the following values: 120/4, 120/2, 120x2, 120x4, 120x8 and 120x16. Similarly, JFNK is tested for values of γ_{nl} of 0.99, 0.75, 0.5, 0.25, 0.1, 0.01 and 0.001. As we will see, these values of N_{sub} and γ_{nl} cover the whole spectrum of inaccurate solutions to the most accurate solution possible for a given Δx and a given Δt. Based on these results, we will define a metric in order to compare the computational efficiency of the JFNK solver to the one of the EVP model. We focus on the 10-km resolution simulations but occasionally refer to the results on the other grids.

6.1. Accuracy of the JFNK and EVP approximate solutions

Figures 2a and 2b show the 10-km resolution thickness and velocity fields on 18 January 2002 00Z as simulated by the Picard solver. We refer to these fields as the reference solution.

Figure 2: Thickness (a) and velocity (b) fields at 10-km resolution on 18 January 2002 00Z obtained with the Picard solver with $\Delta t = 10s$ and $\gamma_{nl} = ^{-6}$. These correspond to the reference solution. For clarity, the thickness is capped to 4 m and one velocity vector out of a hundred is plotted.

For comparing approximate solutions obtained with JFNK or the EVP, we calculated at first the Root Mean Square Difference (RMSD) between a simulated thickness field on 18 January 2002 00Z and the reference thickness field (Figure 2a). It is interesting to look at this field as thickness acts as an integrator of the residual errors during the 1-day integration. The RMSD results then provided guidance for the remaining experiments described in this paper.

The RMSD are computed for regions where the ice concentration is larger than 50%. As an indication, Figure 3 shows the 10-km resolution ice concentration field on 18 January 2002 00Z as simulated by the Picard solver. The RMSD for JFNK and EVP for different spatial resolutions, advective time steps and γ_{nl} (JFNK) or N_{sub} (EVP) are shown in Figure 4. Consistent with what is expected, the differences with the reference solution decrease as the termination criterion γ_{nl} for JFNK is reduced. Similarly, the differences for the EVP model decrease when increasing N_{sub}. Also consistent with what we expect, the RMSD decreases as the advective time step is diminished. For both JFNK and the EVP, the RMSD curves flatten out. This means that, at this point, the RMSD are then mostly a consequence of the large advective time steps. For both solvers, the minimum RMSD level increases with spatial resolution (for the same Δt). It is observed that for a given Δt and a given Δx, the minimum RMSD is always at a higher level with the EVP model. In other words, the approximate solution obtained with JFNK is always more accurate than the one obtained with the EVP (when the solvers iterate sufficiently to reach their respective saturated RMSD level). Importantly, the difference between the EVP approximate solution and the

JFNK approximate solution gets more pronounced as the grid is refined.

Figure 3: Ice concentration field at 10-km resolution on 18 January 2002 00Z obtained with the Picard solver with $\Delta t = 10s$ and $\gamma_{nl} = ^{-6}$

To have an idea of the geographical distribution of these differences, Figure 5a and 5c show respectively the differences between the JFNK approximate solution with γ_{nl}=0.5 and $\gamma_{nl} = 10^{-3}$ and the reference solution. The advective time step is 20 min and Δx=10 km. Figure 5b and 5d are respectively the differences between the EVP approximate solution with $N_{sub} = 120$ and $N_{sub} = 1920$ and the reference solution. Values of γ_{nl}=0.5 and $N_{sub} = 120$ are chosen to show inaccurate solutions while $\gamma_{nl} = 10^{-3}$ and $N_{sub} = 1920$ demonstrate the most accurate solutions that can be obtained by a solver for a given Δt and Δx. Note that decreasing γ_{nl} for JFNK from 10^{-2} to 10^{-3} or increasing N_{sub} from 960 to 1920 have little impact on their respective approximate solution (i.e, there is no need to further decrease γ_{nl} or further increase N_{sub}).

Tightening up the convergence criterion from γ_{nl}=0.5 to $\gamma_{nl} = 10^{-3}$ leads to a clear benefit for the JFNK solver. Similarly, a larger number of subcycles for the EVP provides a better approximate solution. However, the errors do not decrease to the level of errors obtained with JFNK. Even with $N_{sub} = 1920$, the EVP leads to differences as large as 75 cm compared to the reference solution (for a reference solution of 2.32 m at that location). This can be compared to a maximum difference of 5 cm with the JFNK solver (for a reference solution of 4.07 m at that location).

a b

Figure 4: RMSD between the approximate solution (thickness) obtained with JFNK and the reference solution at 40 km (a), 20 km (c) and 10 km (e) and RMSD between the approximate solution (thickness) obtained with the EVP and the reference solution at 40 km (b), 20 km (d) and 10 km (f).

We now turn to the velocity fields. Figures 6a and 6c show respectively the difference between the velocity field simulated by JFNK on 18 January 2002 00Z with γ_{nl}=0.5 and $\gamma_{nl} = 10^{-3}$ and the reference solution. The time

Figure 5: Difference between the thickness field obtained with JFNK with γ_{nl}=0.5 (a) or $\gamma_{nl} = 10^{-3}$ (c) and the reference solution. Difference between the thickness field obtained with the EVP with $N_{sub} = 120$ (b) or $N_{sub} = 1920$ (d) and the reference solution. The advective time step for the JFNK and EVP solvers is 20 min. To see the details, the thickness differences are capped to ±2.5 cm.

step is 20 min. Similarly, the approximate solutions for the EVP with respectively 120 and 1920 subcycles minus the reference solution are shown on Figures 6b and 6d. The same reference vector (2 cm s^{-1}) is used for Figures 6a, 6b, 6c and 6d. Even though the EVP approximate solution (not shown) resembles the reference solution, some differences are present. With 120 subcycles, the EVP approximate solution has significant errors over all the domain. Increasing the number of subcycles from 120 to 1920 improves agreement with the reference solution but there are still some regions with errors of O(1 cm s^{-1}). Decreasing γ_{nl} from 0.5 to 10^{-3} for JFNK leads to errors an order of magnitude smaller than the ones associated with the EVP with $N_{sub} = 1920$.

a b

Figure 6: Difference between the velocity field obtained with JFNK with γ_{nl}=0.5 (a) or $\gamma_{nl} = 10^{-3}$ (c) and the reference solution. Difference between the velocity field obtained with the EVP with $N_{sub} = 120$ (b) or $N_{sub} = 1920$ (d) and the reference solution. The advective time step for the JFNK and EVP solvers is 20 min.

Some of the differences between the EVP velocity field and the reference solution are due to the different thickness and concentration fields after one day of integration. To investigate this impact, a new 10 km resolution reference solution was produced keeping the thickness and concentration fields constant (only the wind forcing varies) during the 1-day integration. First, to quantify the quality of the JFNK and EVP approximate solutions on 18 January 2002 00Z, the RMS of the magnitude of the velocity difference (RMSDv) between the JFNK or the EVP approximate solution and the new reference solution was calculated. The time step for the JFNK and EVP runs is 20 min. The RMSDv for the JFNK (in blue) as a function of γ_{nl}

and the RMSDv for the EVP (in black) as a function of N_{sub} are shown in Figure 7a. Again, the JFNK solver leads to smaller differences than the EVP model when compared to the reference solution. A smaller γ_{nl} appears to be needed to reach the saturated RMSDv level as compared to the previous RMSD thickness results. Figure 7b shows an example of the geographical distribution of these differences for the EVP model. It shows the difference between the EVP velocity field on 18 January 2002 00Z with N_{sub}=1920 and the new reference solution. Figure 7b can be compared with Figure 6d (case with advection, N_{sub}=1920). Qualitatively speaking, the conclusions remain the same. The differences are of the same order of magnitude (O(1 cm s^{-1})) and the largest ones are located in the same regions.

a b

Figure 7: a) RMS of the magnitude of the velocity difference between the JFNK (in blue) or the EVP (in black) approximate solution and the reference solution. b) Difference between the velocity field obtained with the EVP with N_{sub} = 1920 and the reference solution. The time step for the JFNK and the EVP solvers is 20 min and the spatial resolution is 10 km. For these experiments, the JFNK, EVP and reference solutions were obtained with the advection turned off.

We now go back to the experiments with advection. One might argue that these differences between the EVP velocity field and the reference solution are small. However, small errors on the ice drift do have a large impact on the deformations. Figure 8 demonstrates this. Figures 8a and 8b show respectively the shear strain rate (second strain rate invariant) and the divergence simulated by the Picard solver (the reference solution) on the 10-km grid. The same fields simulated with the EVP solver with N_{sub} = 120 are shown on Figures 8c and 8d while Figures 8e and 8f are for N_{sub} = 1920. The advective time step for the EVP is Δt=20 min. Similarly to what is shown in Hunke [11], increasing N_{sub} eliminates noise in the deformation fields. An example of this can be clearly seen if we zoom on the area north of Greenland (Figures 9a and 9b). In the southern part of this region, the noise disappears in the divergence field and the ice becomes very rigid (as seen in the reference solution). However, in the region further north, the noise disappears but is replaced by bands of convergence that are not seen in the reference solution. By comparing Figures 8e and 8f to Figures 8a and 8b, it is obvious that these additional deformations are seen at many places in the domain.

These arch-like deformations in the EVP approximate solution are similar to the ones obtained by Maslowski and Lipscomb [33] with their 9-km EVP model. Hence, the EVP solver with N_{sub} =1920 captures the general pattern of deformations but leads to additional shear lines and zones of strong divergence/convergence when compared to the reference solution. This is consistent with the results of Losch and Danilov [13]: the EVP simulates a weaker ice cover as it deforms more easily. The shear and divergence fields simulated by JFNK ($\gamma_{nl} = 10^{-3}$, Δt=20 min) are very similar to the reference solution deformation fields (not shown).

a b

Figure 8: Shear (a) and divergence (b) at 10-km resolution obtained with the Picard solver with $\gamma_{nl} = 10^{-06}$ and and advective time step of 10 s (the reference solution) on 18 January 2002 00Z. Shear (c) and divergence (d) obtained with the EVP with 120 subcycles. Shear (e) and divergence (f) obtained with the EVP with $N_{sub} = 1920$ on 18 January 2002 00Z. The advective time step for the EVP solver is 20 min. For clarity, the shear is capped to 0.2 day^{-1} and the divergence to $\pm$0.05 day^{-1}.

Figure 9: Divergence north of Greenland as simulated by the EVP with $N_{sub} = 120$ (a) and with $N_{sub} = 1920$ (b) on 18 January 2002 00Z. The advective time step is 20 min. To see the details, the divergence is capped to $\pm$0.025 day^{-1}.

We also performed the following simulations to further investigate the presence of extra deformations in the EVP approximate solution. The model was run for 10 days (17-27 January 2002) with either the JFNK or EVP solver. The spatial resolution is 10 km and Δt=20 min. Because it is a longer simulation, exceptionally this experiment includes thermodynamic processes. Statistics of deformations were calculated over the whole period based on instantaneous deformations analyzed every 12 hours. Similar to what is done in Girard et al. [18], we calculated the Probability Density Function (PDF) of the absolute divergence $|D|$ over a subdomain located in the Arctic Ocean. To avoid coastal effects, the size of the subdomain (1900 km x 1800 km) was chosen such that the grids cells are at least 100 km away from the land.

Bins of constant size of $2 \times 10^{-4}\text{day}^{-1}$ were used to produce the PDF. The first bin includes the values of $|D|$ between 0 and $2 \times 10^{-4}\text{day}^{-1}$, the second one between $2 \times 10^{-4}\text{day}^{-1}$ and $4 \times 10^{-4}\text{day}^{-1}$ and so on. With $X_i = \{1, 3, 5, ..\} \times 10^{-4}\text{day}^{-1}$ giving the midpoint value of each bin and Y_i representing the fraction of $|D|$ values in each bin, Figure 10 shows $\log(Y_i)$ as a function of $\log(X_i)$. The blue curve in Figure 10 shows the PDF for JFNK with $\gamma_{nl} = 10^{-3}$ while the red and the black curves are respectively for the EVP solver with either 120 or 1920 subcycles.

Figure 10: PDF of the absolute divergence for JFNK with $\gamma_{nl} = 10^{-3}$ (in blue), EVP with 120 subcycles (in red) and EVP with 1920 subcycles (in black). For all three simulations, the spatial resolution is 10 km and the advective time step is 20 min. The statistics of the absolute divergence (with bins of $2 \times 10^{-4}\text{day}^{-1}$) were calculated over a 1900 km x 1800 km subdomain centered in the Arctic Ocean.

These results confirm what can be qualitatively observed on Figure 8: the EVP simulates a weaker ice cover as it deforms more easily (both in convergence and divergence, not shown). Interestingly, the PDF for the EVP model changes significantly when increasing the number of subcycles from 120 to 1920 as it gets closer to a fat tailed distribution. Consistent with the results of Lemieux and Tremblay [8] with a Picard solver, we find that the PDF of deformations depends strongly on the level of numerical convergence. It is beyond the scope of this paper to investigate the impact of these extra deformations in the EVP approximate solution on ice growth, but we speculate that the EVP solver leads to more ice production than an implicit solver (because openings in the ice cover strongly affect the ice growth).

The conclusions given in this section are robust. The same RMSD calculation was repeated for two different dates (30 January 2002 and 15 September 2002). Again, results show that the RMSD for EVP is always higher than the saturated level obtained with JFNK (not shown). Note that because the ice cover is less compact during the September test case, the EVP RMSD saturated value is closer to the JFNK saturated value results than it is for the winter test cases. We also verified that these conclusions do not depend on the treatment of the off-diagonal terms (Coriolis and part of the water drag term) for our C-grid implementation. To do so, the Coriolis parameter and the water drag turning angle were set to zero (for the JFNK, EVP

and reference solutions). Comparing again the JFNK and EVP approximate solutions to this new reference solution, our conclusions remain the same: JFNK is more accurate than the EVP (not shown). Finally, conclusions are also unaffected when capping the viscous coefficients to the value proposed by Hunke [11], i.e, by setting the lower limit of $\triangle$ in equation (8) to $10^{-11}\mathrm{s}^{-1}$.

6.2. Computational efficiency

As this work involves serial algorithms, we only briefly comment on the computational efficiencies of the JFNK and EVP solvers. We used the RMSD of the thickness field to investigate the computational efficiency (with Δt=20 min). Our tests show that, for the four spatial resolutions tested, the EVP and JFNK solvers require roughly the same CPU time to reach their respective saturated level (not shown, in fact we calculated the time required for the RMSD to be within 5% of the saturated level). As the spatial resolution is increased, N_{sub} needs to be increased for the EVP solver to reach the minimum RMSD. Even though the required γ_{nl} for JFNK is roughly constant with resolution (~ 0.2), the number of Krylov iterations increases (this explains why the computational efficiencies are comparable for the four spatial resolutions). Hence, for a given Δt and a given Δx, the EVP and JFNK solvers take the same CPU time to reach their respective most accurate solution, but the solution obtained with JFNK always exhibits a lower RMSD value.

7. Discussion

Because of residual elastic waves, the approximate solution calculated with the EVP solver has notable differences with the reference solution. In the experiments described in section 6, the damping time scale was set to the value proposed in the CICE documentation (T=$0.36\Delta t$). Following the notion that the EVP approximate solution converges to the VP solution in the limit of vanishing elastic waves, a better approximation should be obtained with the EVP model by decreasing the damping time scale. We investigate this idea with two additional sets of experiments with the EVP model, in which the damping time scale is reduced to a third and a tenth of the standard value. For these experiments, the 10-km grid is used with an advective time step of 20 min. The black, blue and red curves in Figure 11 respectively

show the RMSD between the EVP with T, T/3 and T/10 and the reference solution. As a reference, the RMSD saturated level for the JFNK solver on the 10-km grid with Δt=20 min is shown as the dashed line.

Figure 11: RMSD between the approximate solution obtained with the EVP and the reference solution for three different damping time scales. The spatial resolution is 10 km and the advective time step is 20 min. The dashed line shows the saturated RMSD level of the JFNK solver.

With decreasing damping time scale, the RMSD saturated level approaches the one obtained with the JFNK solver (represented by the dashed line). However, to resolve the smaller damping time scale, the subcycling time step has to be reduced [11]. Reducing the damping time scale significantly is unpractical and the way the EVP solver is used is therefore a tradeoff between computational efficiency (and a very good parallel scaling) and the presence of residual elastic waves. Our conclusions are in agreement with the results of Losch and Danilov [13]: the EVP approximate solution converges slowly to the VP solution.

For a given Δt and a given Δx, the EVP and JFNK solvers take the same CPU time to reach their respective most accurate solution (note that the JFNK approximate solution is closer to the reference solution than the EVP one for all the spatial resolutions tested). It is important, however, to point out that all efficiency statements are based on serial code. At this point, we expect that the EVP solver scales better with the number of processors because our preconditioner involves an LSOR [7]. Current work is focusing on implementing a multi-grid [34] based preconditioner, and eventually using a parallel multilevel preconditioner such as ML available in the Trilinos library [29]. A similar numerical framework (JFNK + the Trilinos library) has been developed for ice sheet modeling and preliminary results show very good scaling with the number of processors [35].

As mentioned earlier, the VP formulation with an elliptical yield curve and a normal flow rule (the standard VP rheology) is contentious. Recent work questions its ability to properly simulate the sea ice deformations (e.g., [16, 17, 18]). Some authors argue that a VP formulation requires a different yield curve and a different flow rule to improve its representation of sea ice

deformations [17]. We argue that a JFNK solver should be preferred over the EVP model for testing this idea. Indeed, testing different VP rheologies would be hampered by the residual elastic waves in the EVP approximate solution as one would be unable to differentiate between effects of a specific rheology (yield curve and flow rule) and effects of numerical noise.

The implicit framework of the JFNK solver represents another advantage. Lipscomb et al. [36] demonstrated analytically that the splitting in time between the momentum and the continuity equations can lead to unphysical solutions when the advective time step is too large: a solution exists but it is inconsistent with the forcing conditions. Numerical experiments showed that sea ice models run into this fundamentally numerical problem as the grid is refined, so that the approximate solution can even blow up [36]. This problem is caused by the explicit treatment of the ice strength in the momentum equation (as done in almost all the sea ice models). We have not observed such instability in our model, probably because we use a very diffusive upstream advection scheme and a two-thickness category model (as opposed to more sophisticated thickness distribution approach).

The instability issue related to the splitting in time approach clearly needs attention as models are run at increasingly higher spatial resolution. Even though Lipscomb et al. [36] proposed a way to mitigate this problem by modifying the ridging scheme, we think a different numerical treatment could further improve the stability and offer more versatility for formulating the ridging scheme. As the JFNK solver is based on an implicit approach, it is naturally suited for resolving this issue within a fully-implicit treatment (similar to the strength implicit model of Hutchings et al. [37]) or using implicit/explicit time integration techniques [38].

In Lemieux et al. [9], we have shown that both the Picard and JFNK solvers can have failures (i.e., a solver does not reach the termination criterion before the maximum allowed number of iterations). For the same advective time step, the number of failures increases as the grid is refined. The JFNK solver seems to be particularly sensitive at high resolution. We erroneously speculated that the increased number of failures with resolution was related to the small-scale sea ice deformations. Here, we report to the contrary that in a thorough analysis of failures, we found that most of them are located near a coast in regions where the thickness and concentration

fields vary significantly from one grid cell to the next. Hence, these failures relate to the issue described by Lipscomb et al. [36] and further motivate the implementation of a fully-implicit solver or the use of an implicit/explicit time integration.

8. Conclusion

We have compared the convergence properties (accuracy of the solution and computational efficiency) of a recently developed Jacobian-free Newton-Krylov (JFNK) serial algorithm to the ones of the widely used Elastic-Viscous-Plastic (EVP) model for solving the sea ice momentum equation with a VP formulation. To do so, a reference VP solution was calculated by using a very small advective time step (10 s) and a tight nonlinear convergence criterion. A Picard scheme was used as an independent solver in order to obtain this reference solution. Tests were then performed with JFNK and the EVP solver at 10, 20, 40 and 80-km spatial resolutions and using advective time steps of 10, 20 and 30 min.

For both solvers, the Root Mean Square Difference (RMSD) between a solver's simulated thickness field and the reference solution decreases when the convergence criterion (for JFNK) is tightened up or when more subcycles (for EVP) are used. The RMSD eventually flattens out because the errors are then a consequence of the large advective time step, but the RMSD for the EVP flattens out at a higher level than for the JFNK solver. This is the case for all advective time steps, when both solvers use the same advective time step. The differences between the EVP and JFNK approximate solutions increase as the grid is refined.

Using the RMSD to investigate the computational efficiency, results show that the JFNK and EVP solvers require about the same CPU time to reach their respective RMSD saturated level, but the JFNK most accurate solution is always closer to the reference solution than is the EVP one. For a given advective time step, it is possible to improve the accuracy of the EVP approximate solution by decreasing the damping time scale. Unfortunately, a smaller damping time scale needs to be resolved by a shorter subcycling time step, so that overall the computational efficiency of the EVP solver is decreased. Consistent with the results of Losch and Danilov [13], we conclude

that the EVP converges slowly to the VP solution. It is however known that the EVP model scales very well with the number of processors [7]. While some existing JFNK parallel codes show very good scaling (e.g., [35]), it remains to be seen how our JFNK implementation will behave in a parallel environment.

Because of residual elastic waves, the velocity field calculated with the EVP solver has notable differences with the reference solution. These residual errors are clearly noticeable in the deformation fields. As opposed to the JFNK solver, the deformations simulated on a 10-km grid with the EVP solver exhibit extra shear lines and zones of large divergence/convergence when compared to the reference solution. Results also show that the Probability Density Function (PDF) of the absolute divergence changes significantly between the standard number of subcycles (120) and the more accurate solution obtained with 1920 subcycles. The distribution is then more fat tailed, and gets closer to the PDF obtained with the JFNK solver.

Because it is an implicit method, the JFNK solver opens up new perspectives of solving numerical issues related to time stepping algorithms (as shown in [36]) and quickly changing ice conditions in high resolution models by a fully implicit approach or implicit/explicit time integration techniques [38]. Such approaches are excluded with the EVP solver by construction.

Acknowledgements

We thank Frédéric Dupont, Elizabeth Hunke, William Lipscomb, and Pierre Rampal for interesting discussions. We thank an anonymous reviewer for helpful comments. Special thanks to William Lipscomb for pointing out the instability issue related to the splitting in time and to Elizabeth Hunke for her help while implementing the EVP solver.

References

[1] M. D. Coon, G. A. Maykut, R. S. Pritchard, D. A. Rothrock, A. S. Thorndike, Modeling the pack ice as an elastic-plastic material, AIDJEX Bulletin 24 (1974) 1–105.

[2] W. D. Hibler, A dynamic thermodynamic sea ice model, J. Phys. Oceanogr. 9 (1979) 815–846.

[3] W. D. Hibler, A Viscous Sea Ice Law as a Stochastic Average of Plasticity, J. Geophys. Res. 82 (27) (1977) 3932–3938.

[4] C. F. Ip, W. D. Hibler, G. M. Flato, On the effect of rheology on seasonal sea-ice simulations, Ann. Glaciol. 15 (1991) 17–25.

[5] J. Zhang, W. D. Hibler, On an efficient numerical method for modeling sea ice dynamics, J. Geophys. Res. 102 (C4) (1997) 8691–8702.

[6] C. Paniconi, M. Putti, A comparison of Picard and Newton iteration in the numerical solution of multidimensional variably saturated flow problems, Water Resour. Res. 30 (12) (1994) 3357–3374.

[7] E. C. Hunke, Y. Zhang, A comparison of sea ice dynamics models at high resolution, Mon. Wea. Rev. 127 (1999) 396–408.

[8] J.-F. Lemieux, B. Tremblay, Numerical convergence of viscous-plastic sea ice models, J. Geophys. Res. 114 (2009) C05009, doi: 10.1029/2008JC005017.

[9] J.-F. Lemieux, B. Tremblay, J. Sedláček, P. Tupper, S. Thomas, D. Huard, J.-P. Auclair, Improving the numerical convergence of viscous-plastic sea ice models with the Jacobian-free Newton Krylov method, J. Comput. Phys. doi:10.1016/j.jcp.2009.12.011.

[10] E. C. Hunke, J. K. Dukowicz, An elastic-viscous-plastic model for sea ice dynamics, J. Phys. Oceanogr. 27 (1997) 1849–1867.

[11] E. C. Hunke, Viscous-plastic sea ice dynamics with the EVP model: linearization issues, J. Comput. Phys. 170 (2001) 18–38.

[12] M. Losch, D. Menemenlis, J.-M. Campin, P. Heimbach, H. Hill, On the formulation of sea-ice models. Part 1: Effects of different solver implementations and parameterizations, Ocean Model. 33 (2010) 129–144, doi:10.1016/j.ocemod.2009.12.008.

[13] M. Losch, S. Danilov, On Solving the Momentum Equations of Dynamic Sea Ice Models with Implicit Solvers and the Elastic-Viscous-Plastic Technique, Ocean Model. 41 (2012) 42–52, doi: 10.1016/j.ocemod.2011.10.002.

[14] E. C. Hunke, W. H. Lipscomb, CICE: the Los Alamos sea ice model documentation and software user's manual version 4.1 Los Alamos, NM, Los Alamos National Laboratory. (Tech. Rep. LA-CC-06-012.).

[15] C. Konig Beatty, D. M. Holland, Modeling landfast sea ice by adding tensile strenght, J. Phys. Oceanogr. 40 (2010) 185–198.

[16] R. Kwok, E. C. Hunke, W. Maslowski, D. Menemenlis, J. Zhang, Variability of sea ice simulations assessed with RGPS kinematics, J. Geophys. Res. 113 (2008) C11012, doi:10.1029/2008JC004783.

[17] K. Wang, C. Wang, Modeling linear kinematic features in pack ice, J. Geophys. Res. 114 (2009) C12011, doi:10.1029/2008JC005217.

[18] L. Girard, J. Weiss, J. M. Molines, B. Barnier, S. Bouillon, Evaluation of high-resolution sea ice models on the basis of statistical and scaling properties of Arctic sea ice drift and deformation, J. Geophys. Res. 114 (C08015), doi:10.1029/2008JC005182.

[19] L. Girard, S. Bouillon, J. Weiss, D. Amitrano, T. Fichefet, V. Legat, A new modeling framework for sea-ice mechanics based on elasto-brittle rheology, Ann. Glaciol. 52 (57) (2011) 123–132.

[20] P. Rampal, J. Weiss, D. Marsan, R. Lindsay, H. Stern, Scaling properties of sea ice deformation from buoy dispersion analyses, J. Geophys. Res. 113 (C03002), doi:10.1029/2007JC005066.

[21] H. Schreyer, D. Sulsky, L. Munday, M. Coon, R. Kwok, Elastic-decohesive constitutive model for sea ice, J. Geophys. Res. 111 (C11S26), doi:10.1029/2005JC003334.

[22] B. Tremblay, L. A. Mysak, Modeling sea ice as a granular material, including the dilatancy effect, J. Phys. Oceanogr. 27 (1997) 2342–2360.

[23] M. G. McPhee, Ice-ocean momentum transfer for the AIDJEX ice model, AIDJEX Bulletin 29 (1975) 93–111.

[24] J. Dukowicz, Comments on the "stability of the viscous-plastic sea ice rheology", J. Phys. Oceanogr. 27 (1997) 480–481.

[25] J.-F. Lemieux, B. Tremblay, S. Thomas, J. Sedláček, L. A. Mysak, Using the preconditioned Generalized Minimum RESidual (GMRES) method to solve the sea-ice momentum equation, J. Geophys. Res. 113 (2008) C10004, doi:10.1029/2007JC004680.

[26] D. A. Knoll, D. E. Keyes, Jacobian-free Newton-Krylov methods: a survey of approaches and applications, J. Comput. Phys. 193 (2004) 357–397.

[27] Y. Saad, A flexible inner-outer preconditioned GMRES algorithm, SIAM J. Sci. Comput. 14 (2) (1993) 461–469.

[28] S. C. Eisenstat, H. F. Walker, Choosing the forcing terms in an inexact Newton method, SIAM J. Sci. Comput. 17 (1996) 16–32.

[29] M. Leroux, Trilinos: an object-oriented software framework for the solution of large-scale-complex, multiphysics and science problems, http://trilinos.sandia.gov Albuquerque, NM, Sandia National Laboratory.

[30] P. R. McHugh, J. D. Ramshaw, Damped artificial compressibility iteration scheme for implicit calculations of unsteady incompressible flow, Int. J. Numer. Meth. Fl. 21 (1995) 141–153.

[31] E. Kalnay, M. Kanamitsu, R. Kistler, W. Collins, D. Deaven, L. Gandin, M. Iredell, S. Saha, G. White, J. Woollen, Y. Zhu, A. Leetmaa, R. Reynolds, M. Chelliah, W. Ebisuzaki, W. Higgins, J. Janowiak, K. C. Mo, C. Ropelewski, J. Wang, R. Jenne, D. Joseph, The NCEP/NCAR 40-year reanalysis project, Bull. Amer. Meteorol. Soc. 77 (1996) 437–470.

[32] M. Johnson, S. Gaffigan, E. Hunke, R. Gerdes, A comparison of Arctic Ocean sea ice concentration among the coordinated AOMIP model experiments, J. Geophys. Res. 112 (2007) C04S11, doi:10.1029/2006JC003690.

[33] W. Maslowski, W. H. Lipscomb, High resolution simulations of Arctic sea ice, 1979-1993, Polar Res. 22 (2003) 67–74.

[34] W. L. Briggs, V. E. Henson, S. F. McCormick, A multigrid tutorial, SIAM, Philadelphia, PA, 2000.

[35] K. J. Evans, A. G. Salinger, P. H. Worley, S. F. Price, W. H. Lipscomb, J. A. Nichols, J. B. White III, M. Perego, M. Vertenstein, J. Edwards, J.-F. Lemieux, A modern solver interface to manage solution algorithms in the Community Earth System Model, Int. J. High Perform. C. 26 (2012) 54–62, doi:10.1177/1094342011435159.

[36] W. H. Lipscomb, E. C. Hunke, W. Maslowski, J. Jakacki, Ridging, strength, and stability in high-resolution sea ice models, J. Geophys. Res. 112 (C03S91), doi:10.1029/2005JC003355.

[37] J. K. Hutchings, H. Jasak, S. W. Laxon, A strength implicit correction scheme for the viscous-plastic sea ice model, Ocean Model. 7 (2004) 111–133.

[38] S. Y. Kadioglu, D. A. Knoll, A fully second order implicit/explicit time integration technique for hydrodynamics plus nonlinear heat conduction problem, J. Comput. Phys. 229 (2010) 3237–3249, doi: 10.1016/j.jcp.2009.12.039.

Figure

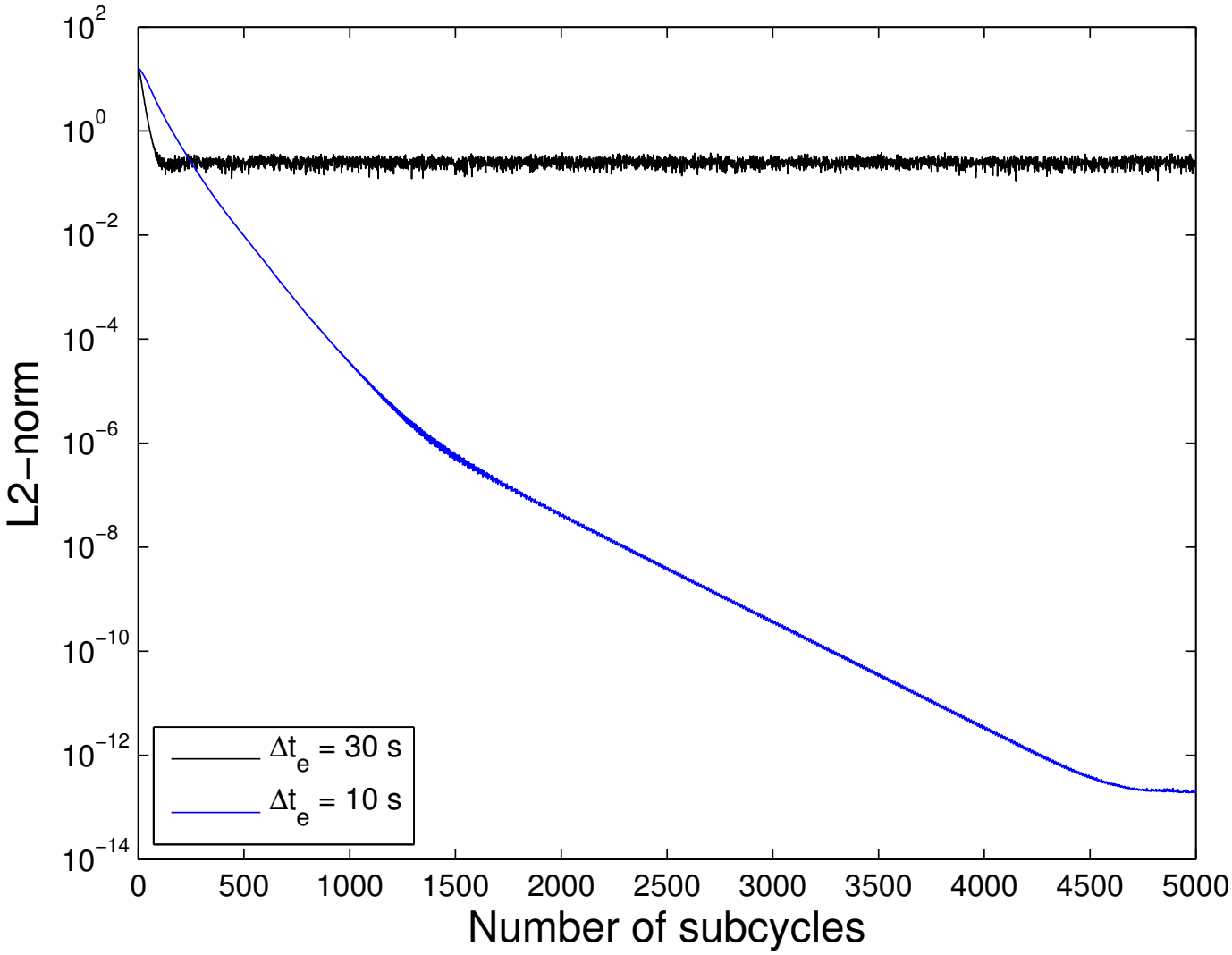
L2−norm
Number of subcycles
Δt_e = 30 s
Δt_e = 10 s
10^2
10^0
10^−2
10^−4
10^−6
10^−8
10^−10
10^−12
10^−14
0
500
1000
1500
2000
2500
3000
3500
4000
4500
5000

Figure

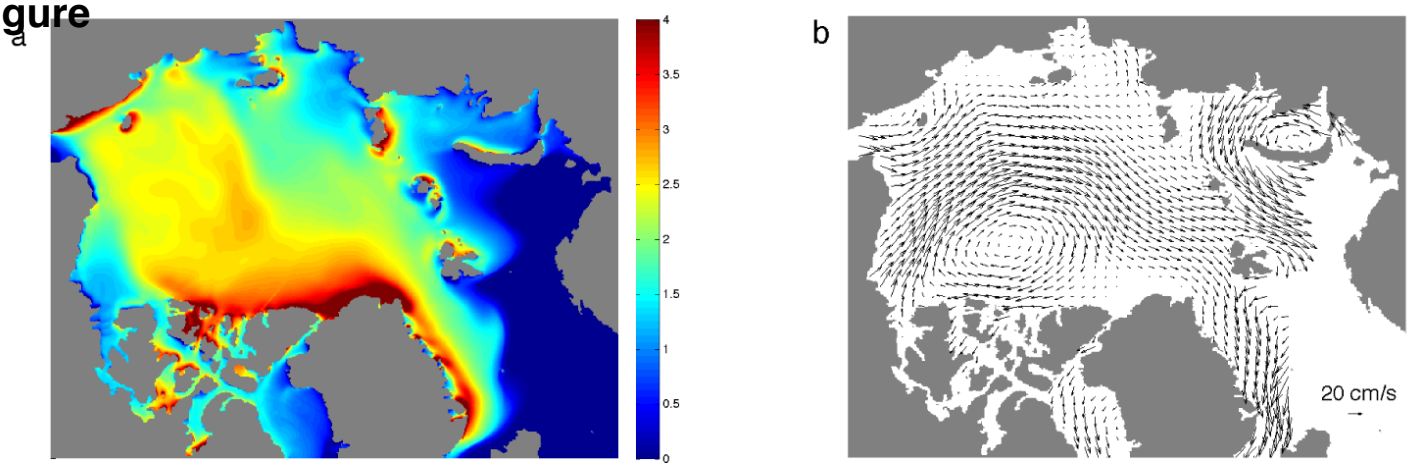

Figure

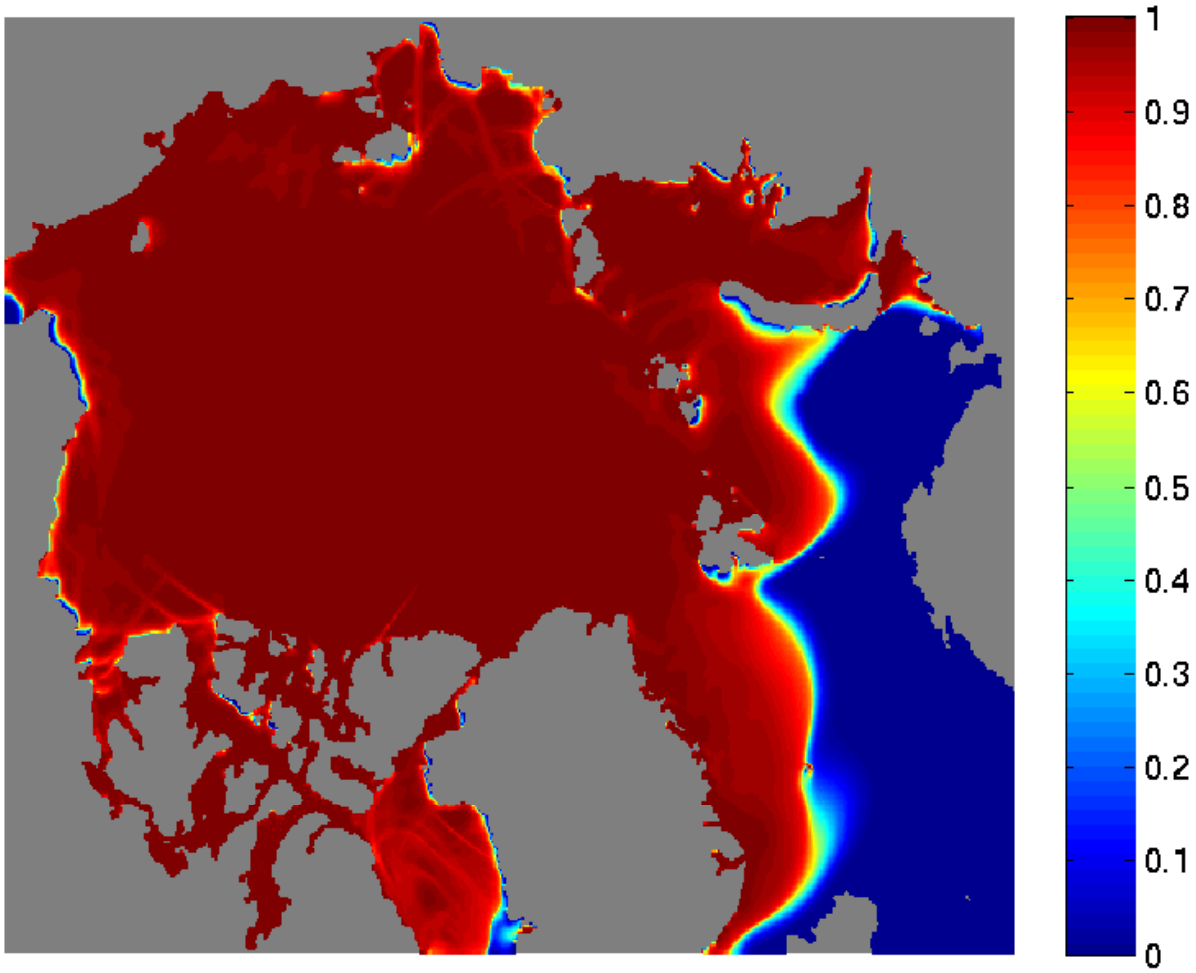

Figure

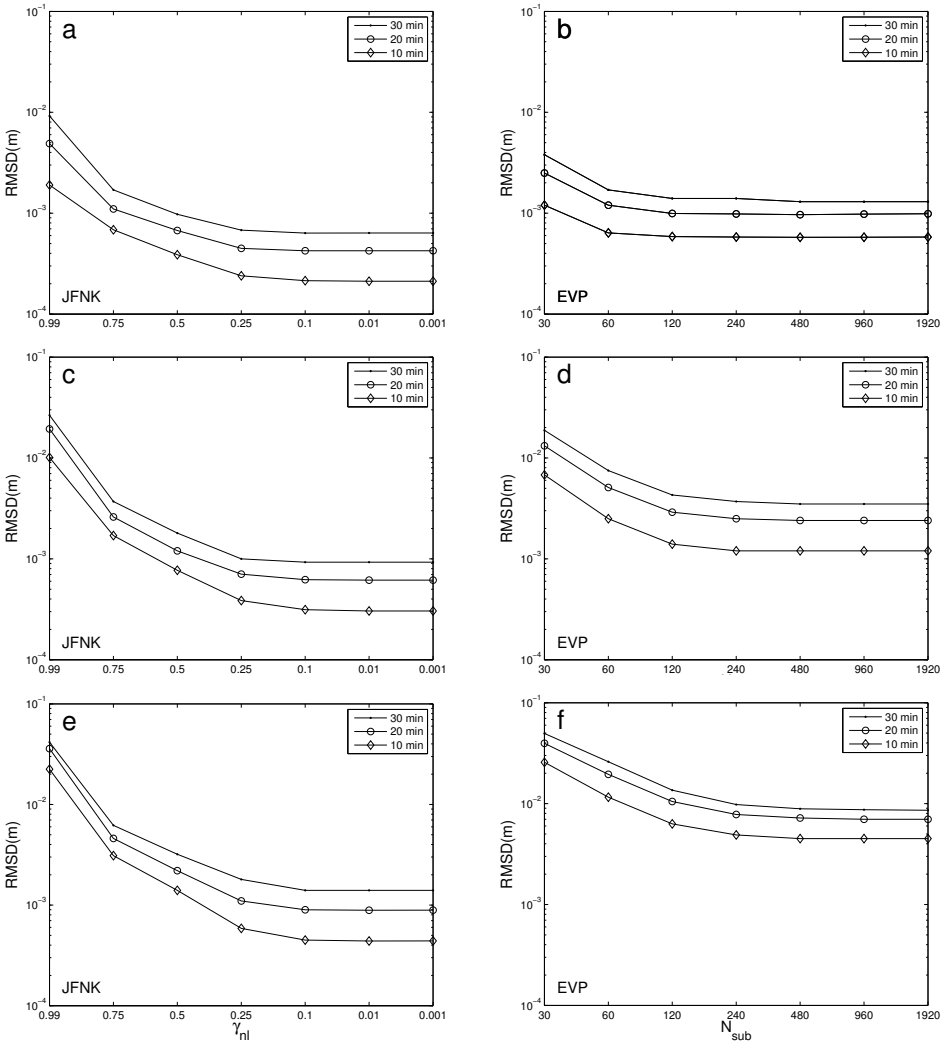
a
b
c
d
e
f
30 min
20 min
10 min
RMSD(m)
JFNK
EVP
0.99
0.75
0.5
0.25
0.1
0.01
0.001
30
60
120
240
480
960
1920
γ_{nl}
N_{sub}

Figure

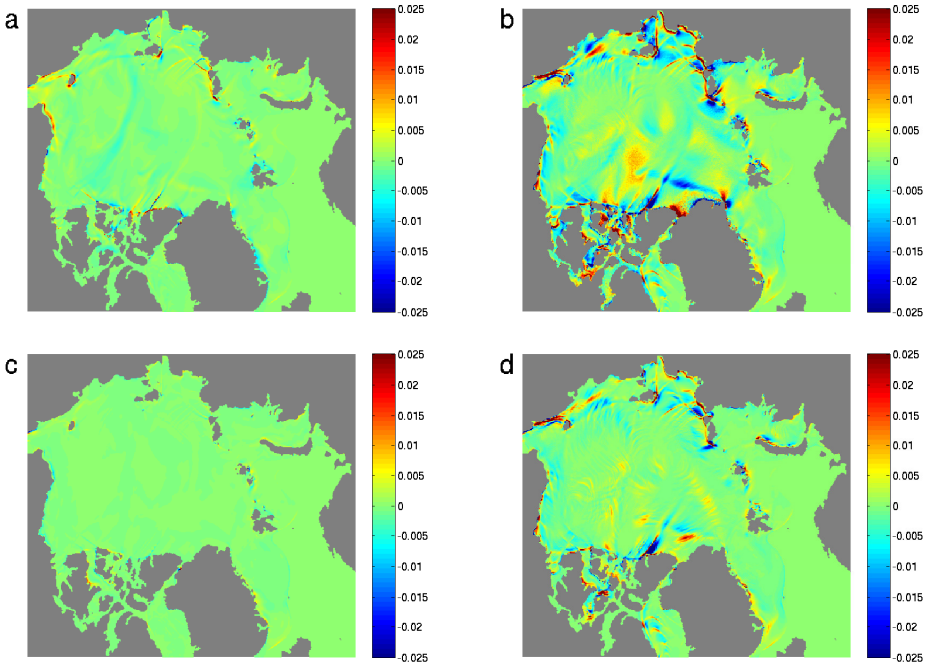

Figure

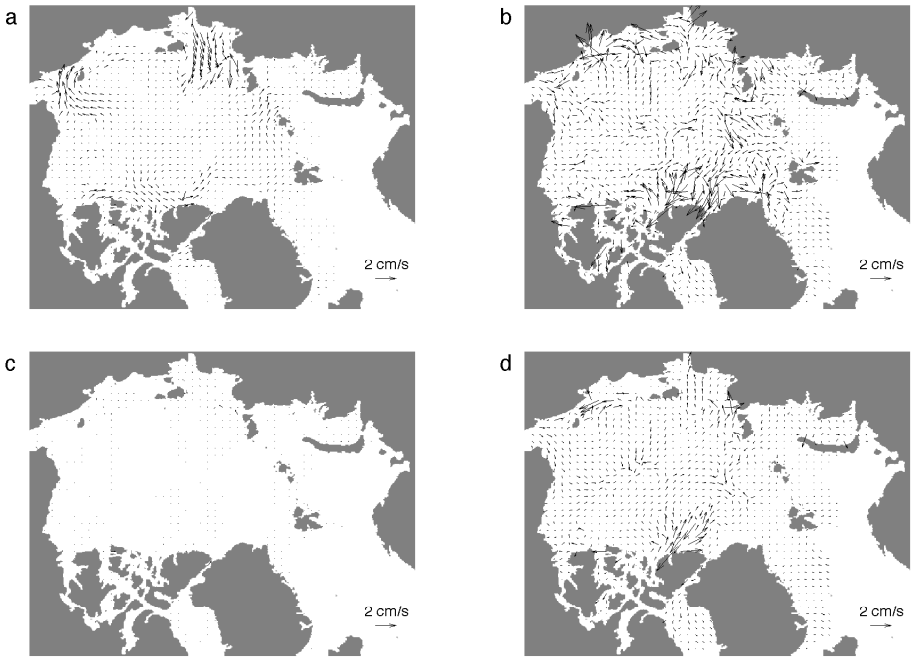

Figure

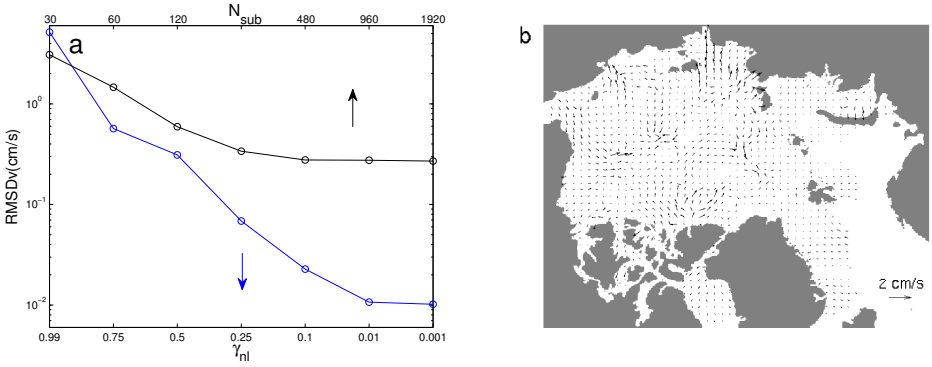
a
b
N_{sub}
30
60
120
480
960
1920
RMSDv(cm/s)
10^{0}
10^{-1}
10^{-2}
0.99
0.75
0.5
0.25
0.1
0.01
0.001
γ_{nl}
2 cm/s

Figure

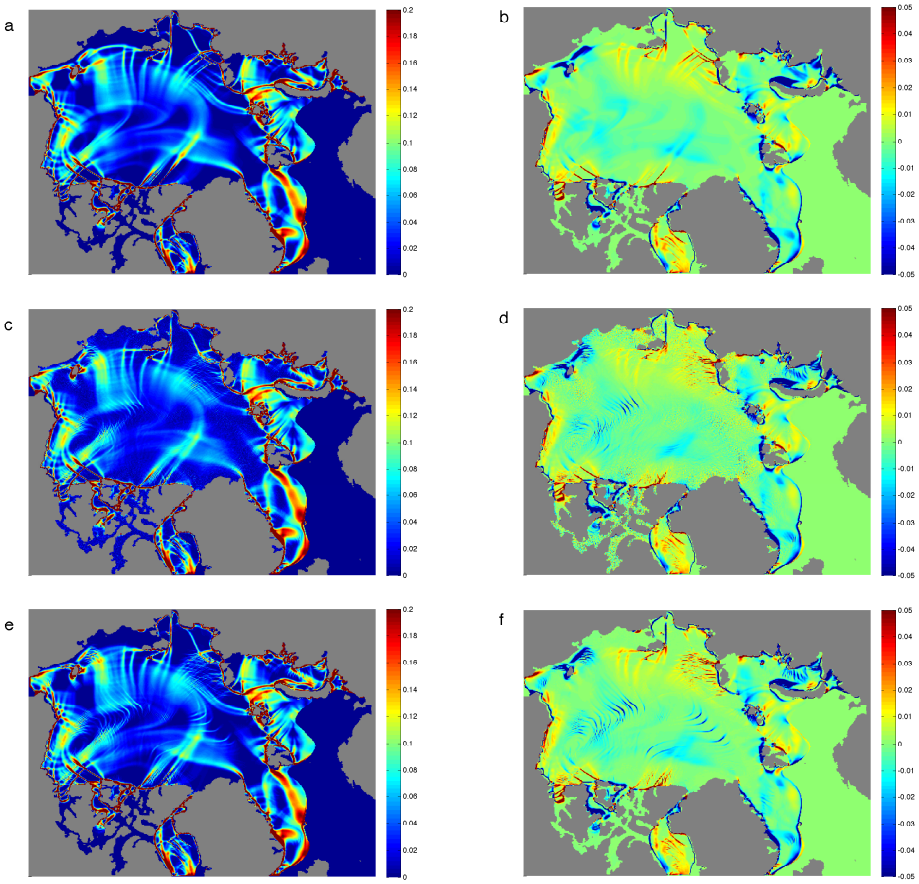

Figure

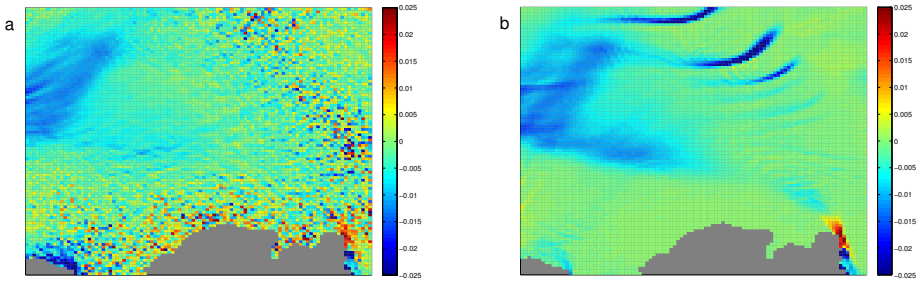

Figure

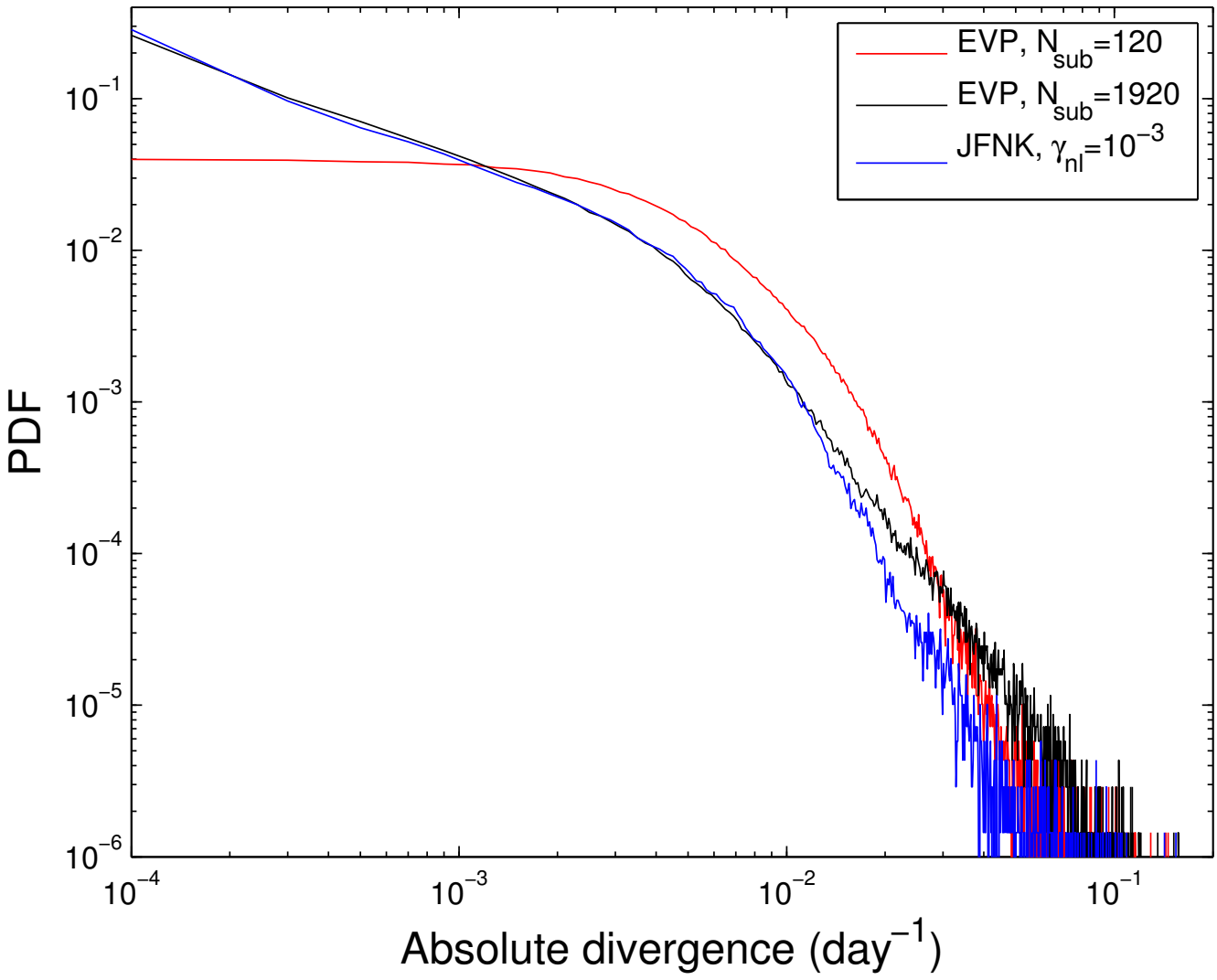
EVP, N_sub=120
EVP, N_sub=1920
JFNK, γ_nl=10^−3
PDF
10^−1
10^−2
10^−3
10^−4
10^−5
10^−6
10^−4
10^−3
10^−2
10^−1
Absolute divergence (day^−1)

Figure

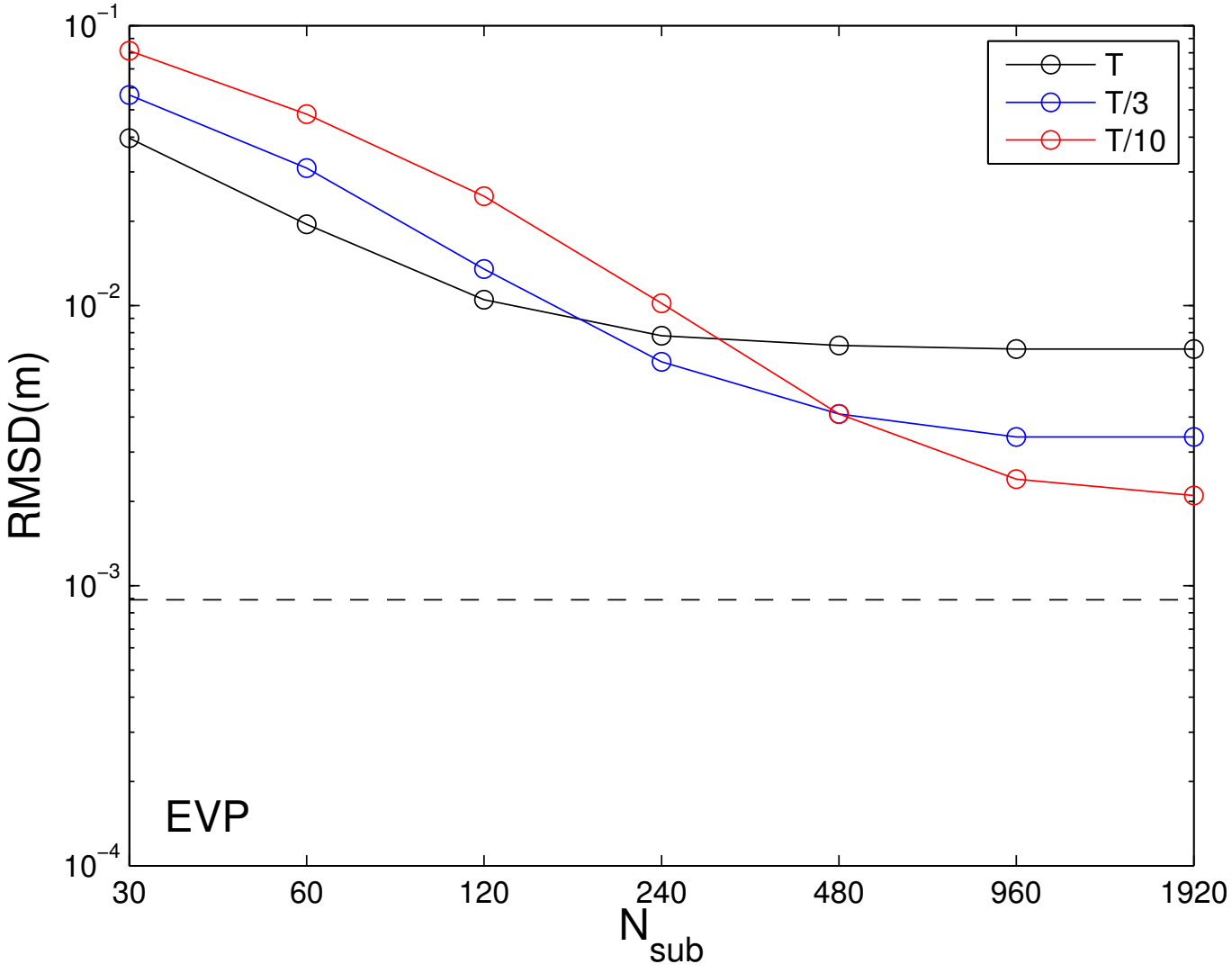
10^{-1}
10^{-2}
10^{-3}
10^{-4}
RMSD(m)
T
T/3
T/10
EVP
30
60
120
240
480
960
1920
N_{sub}